ISOTOPE SELECTIVE MEASUREMENTS IN A LASER INDUCED PLASMA

By

LESLIE ANTHONY KING

A DISSERTATION PRESENTED TO THE GRADUATE SCHOOL OF THE UNIVERSITY OF FLORIDA IN PARTIAL FULFILLMENT OF THE REQUIREMENTS FOR THE DEGREE OF DOCTOR OF PHILOSOPHY

UNIVERSITY OF FLORIDA

1998

ACKNOWLEDGMENTS

I would like to express my sincere appreciation to my mentor, Jim Winefordner, for his guidance and friendship over the last four years. The research atmosphere he provides with a friendly group of graduate students, visiting professors, and post doctoral researchers has been a wonderful experience for me. I would also like to thank Benjamin Smith for his instruction, advice, and reassurance during my graduate career. This work most certainly would not have been possible without the help of Igor Gornushkin who taught me so much about problem solving and patience.

My appreciation also goes to the members of the JDW research group for their support and friendship. I would especially like to thank Andrea Croslyn, Bryan Castle, Rob Guenard, Cindy Baker, Wendy Clevenger, Dave Rusak, Scott Baker, Dave Besteman, Gretchen Potts, Ricardo Aucelio, and Dimitri Pappas. I would also like to thank Kobus Visser, Piet Walters, Oleg Matveev, and Nico Omenetto for teaching me so much about spectroscopy during their visits. I must express my gratitude to Guy Weerasekera for his friendship and support during my entire college and graduate career. A friend as special as Guy is truly a rare treasure.

I would also like to thank the people at Georgia College who encouraged me to attempt graduate school and prepared me for the experience: Dave Baarda, Ken McGill, Doug Pohl, and Betty Jo Dunn. I also appreciate their continuing concern and support.

My family has always been the real force behind my accomplishments. I am very fortunate to have my father, mother, and sister, Ashley, to always believe that I can succeed. I cannot even begin to express how much their love and support mean to me. I am the luckiest person in the world to have married my best friend, Mark King. I appreciate his love, support, sacrifice, and patience during these first few years of many to come. I would like to say that my inspiration to continue with school has come from God.

I can do all things through Him who strengthens me. (Philippians 4:13)

Finally, I would like to thank the wonderful staff of the chemistry department including Jeanne Karably, without whom none of us could survive, Joe Shalosky, Todd Prox, Steve Miles, Donna Balkom, Jim Deyrup, and Kathryn Williams. I would also like to acknowledge the Texaco Foundation for financial support through the award of a fellowship.

TABLE OF CONTENTS

Abstract of Dissertation Presented to the Graduate School
of the University of Florida in Partial Fulfillment of the
Requirements for the Degree of Doctor of Philosophy

ISOTOPE SELECTIVE MEASUREMENTS IN A LASER INDUCED PLASMA

By

Leslie Anthony King

December, 1998

Chairman: Prof. James D. Winefordner
Major Department: Chemistry

In laser induced plasma spectroscopy (LIPS), a laser beam of sufficient energy is focused onto the surface of a solid sample in order to produce a plasma. The plasma can be monitored by several spectroscopic techniques. However, optical emission spectroscopy has by far been the most popular method of choice. The goal of this work was to evaluate the use of laser excited atomic fluorescence (LEAFS) and laser source atomic absorption spectroscopy (LAAS) as methods to detect species in a laser induced plasma. The advantages of using laser induced plasma spectroscopy are: little sample is needed, no sample preparation for solid samples is required, and the instrumentation is relatively inexpensive.

The figures of merit for LEAFS and LAAS in a plasma were determined for alkali metals in copper and NIST reference materials. Detection limits on the order of ppb were

determined for fluorescence detection and detection limits of ppm were measured for the absorption experiment. The accuracy of these two methods was evaluated by analyzing National Institute of Standards and Technology standard reference materials, and the accuracy of these methods was excellent.

During the course of the experiment to evaluate fluorescence and absorption detection, it was discovered that isotope structure could be resolved in a laser induced plasma. This was further investigated by analyzing the isotopes of lithium in a laser plasma formed on a solid lithium oxalate sample at reduced pressures by laser excited atomic fluorescence. A dye laser was used to probe the 670 nm transition of lithium, and the ^{6}Li and ^{7}Li isotopes were resolved. The lithium isotope ratio was determined to be 12.1 with a RSD of 4%.

The two isotopes of rubidium were resolved in a laser induced plasma by measuring the atomic absorption of each isotope. A narrowband Ti:Sapphire laser was scanned across the isotope transitions, and the spectra recorded. Calibration curves for each isotope were constructed, and the resulting figures of merit are discussed. The rubidium isotope ratio and concentrations were determined in a real geological sample in order to test the applicability of this technique. The line broadening mechanisms which take place in a low pressure laser induced plasma are discussed.

CHAPTER 1
INTRODUCTION

The goal of this work was to evaluate laser excited atomic fluorescence (LEAFS) and laser source atomic absorption spectroscopy (LAAS) as detection schemes for laser induced plasmas (LIP). During the course of this project, it was discovered that some isotope structure could be resolved in the LEAFS and LAAS spectra. Therefore, this project became focused upon measuring and resolving isotopes in a laser induced plasma.

Chapter two provides background information on using laser ablation (LA) as an analytical tool, and information on LA combined with LEAFS and LAAS detection. This chapter concludes by demonstrating some important uses of isotope analysis. The fundamental principles of isotope shifts are discussed in chapter three, as well as the effect of isotope structure on the fluorescence measurements. The initial results from the evaluation of LA-LEAFS and LA-LAAS are given in chapter four. The combination of LEAFS and LAAS detection schemes in a laser induced plasma provides an analytical tool which allows for the direct analysis of solid samples with good precision, limits of detection on the order of ppb and ppm for LEAFS and LAAS, respectively, and excellent accuracy. The isotope selective measurements are reported in chapters five and six. The ^{7}Li and ^{6}Li isotope ratio was measured using LA-LEAFS and the ^{85}Rb and ^{87}Rb isotopes were resolved using LA-LAAS. Isotope selective calibration curves for rubidium were constructed and the analytical figures of merit were determined. Also, the applicability of this technique was evaluated by

measuring the rubidium isotope concentrations and ratios in real geological samples. The possible line broadening mechanisms which occur in the laser induced plasma are also discussed. The applicability of the curve of growth method to analysis of laser induced plasmas is reported in chapter seven, and the conclusions and future work are given in chapter eight. The presentations and publications which have resulted from this work are listed in the Appendix.

CHAPTER 2
BACKGROUND OF LASER INDUCED PLASMA SPECTROSCOPY

Laser Induced Plasmas

Soon after the development of the ruby laser, it was shown that one could cause the breakdown of air by bringing a laser beam into tight focus [1]. This laser induced breakdown process generates an almost totally ionized gas called a laser induced plasma, and analytical methods which utilize this process are called laser induced plasma spectroscopy (LIPS). There are two main mechanisms for electron generation and growth of the plasma. The first mechanism involves absorption of laser radiation by electrons when they collide with neutrals. When the electrons gain sufficient energy, they ionize the gas or solid by impact.

$$e^- + M \rightarrow 2e^- + M^+$$

This process leads to cascade breakdown because the electron concentration increases exponentially with time. Two conditions must be met in order to achieve cascade breakdown (1) there must be an initial electron in the focal volume, and (2) the electrons must acquire an energy which is greater than the ionization energy of the gas [2].

The second mechanism which can occur is called multiphoton ionization. This process involves the simultaneous absorption of enough photons by an atom to cause ionization.

$$M + mh\nu \rightarrow M^+ + e^-$$

If ϵ_I is the ionization potential, then the number of photons, m, must exceed $(\epsilon_I / h\nu+1)$. Both

cascade and multiphoton ionization require high laser irradiances, generally greater than 10^8 W/cm^2 [2].

A representation of the evolution of a laser induced plasma is shown in Figure 2-1. The laser induced plasma is formed when a high energy, short duration laser pulse strikes the surface of a material. There is an instant increase in the surface temperature and vaporization of the sample begins to occur. This process occurs because of the cascade breakdown and multiphoton ionization processes described above. Because the dissipation of energy through the vaporization process is slow relative to the rate at which energy is deposited in the short laser pulse, the underlying layers of material reach critical temperatures and pressures before the surface layer can vaporize. This causes the surface to explode and a plasma to form. The ablated material is ejected from the surface in the form of particles, free electrons, atoms, ions, and droplets. These materials expand at a velocity which is much faster than the speed of sound, so a shock wave is formed in the surrounding atmosphere. After several microseconds, approximately 10 μs, the plasma plume begins to cool down because of collisions with the ambient gas. Plasma temperatures on the order of 10^4-10^5 K and electron number densities on the order of 10^{15}-10^{19} cm^{-3} have been measured [3]. At later plasma lifetimes, approximately 20 μs or later, the plasma starts to decay because of radiative, quenching, and electron-ion recombination processes. These processes lead to the formation of a post-plasma region which contains a high number density of neutral species. Finally, the decay is completed by the formation of clusters, condensation, three-bodied collisions, and diffusion of plasma particles into the surrounding gas. The decay is complete within hundreds

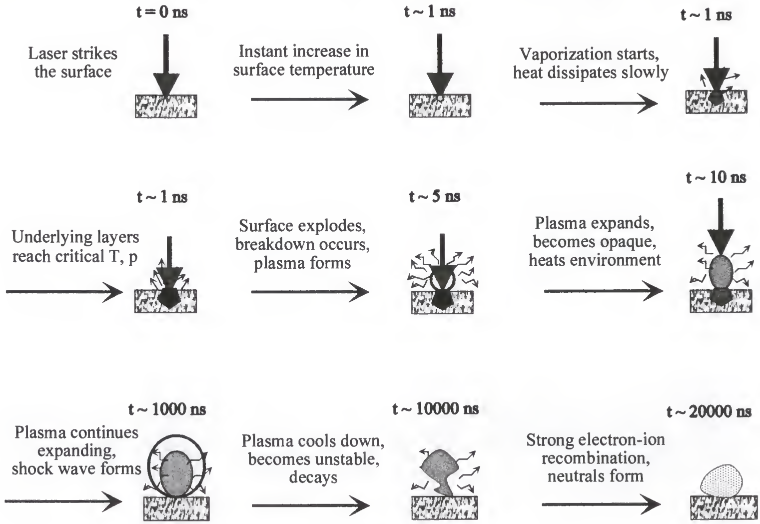

Figure 2-1: The evolution of a laser induced plasma.

of microseconds after the plasma was created [4]. A digitally enhanced photograph of a laser induced plasma is shown in Figure 2-2.

Laser induced plasmas can be combined with several detection schemes including, optical emission spectroscopy (OES), atomic absorption spectroscopy (AAS), and laser induced fluorescence spectroscopy (LIF). There are several advantages of using laser induced plasmas as an analytical tool. Perhaps the biggest advantage is the fact that only optical access to the sample is required for sampling. This feature allows for the use of LIPS in remote sensing applications. Also, there is little or no sample preparation required for solid samples analysis, which is quite attractive versus, for example inductively coupled plasma spectroscopy which requires sample dissolution before analysis. However, there are some problems to overcome with LIPS including variations in the mass ablated from heterogeneous samples which can make quantification difficult. Table 2-1 list the advantages and disadvantages of using laser induced plasmas for analytical purposes.

There are many factors which contribute to the plasma formation, vaporization, and atomization, and all of these contributing factors are not completely understood. The reason for the complexity is due to the large number of variables which influence the ablation process. One such variable is the energy of the ablation laser radiation. Hwang, Teng, Li, and Sneddon give a detailed theoretical consideration of the relationship between laser energy and mass ablated [5]. They were able to predict that the mass ablated should increase with laser energy. They also performed a series of experiments to confirm their theoretical model which indicated an increase in mass ablated up to an energy of 200 mJ.

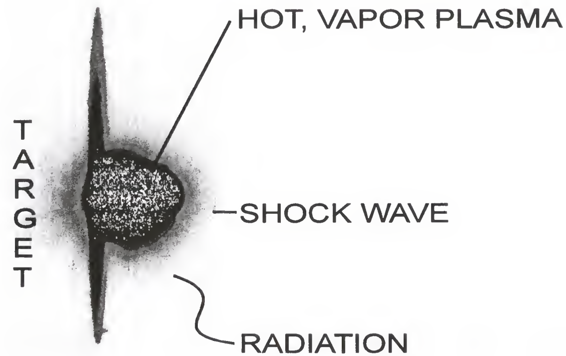

Figure 2-2: Digitally enhanced photograph of a laser induced plasma.

Table 2-1: Advantages and Disadvantages of Laser Induced Plasma Spectroscopy.

Advantages	Disadvantages
1. Minimal or no sample preparation	1. Variation in the mass ablated caused by heterogeneity of the sample matrix
2. Solids, liquids, and gases can be analyzed. Conductive and nonconductive samples can be used	2. Difficulty in obtaining matrix-matched standards.
3. Small amounts of sample are needed	3. Detection limits higher than for standard techniques (ICP-MS)
4. Easy analysis of refractory materials such as ceramics	4. Precision worse than for standard techniques
5. Spatial resolution is possible	5. High energy density laser damages (removes) sample
6. Capability of remote analysis	6. No complete theory exists because of the complex processes involved
7.Simultaneous multielement analysis is possible	

Wisburn, Schechter, Niessner, Schroder, and Kompa reported on the relationship between the signal-to-noise ratio and the ablation laser energy [6]. They showed that the S/N increased with increasing energy up to 150 mJ, at which point the signal-to-noise ratio leveled off.

Another important factor affecting the laser induced plasma process is the ablation laser wavelength. Pinnick et al. reported on the affect of wavelength on the breakdown thresholds [7]. They used a Nd:YAG laser with a doubling crystal in order to obtain ablation

wavelengths of 1064 nm, 532 nm, 355 nm, and 266 nm. They showed a decrease in the threshold value with decreasing wavelength. The wavelength dependence of the breakdown threshold was explained by considering the increasing importance of multiphoton absorption processes at the shorter wavelengths.

The composition and pressure of the surrounding atmosphere as well as the chemical characteristics of the target material greatly affect the breakdown process. Kuzuya, Matsumoto, Takechi, and Mikami studied the effect of atmosphere on the aluminum emission lines from a nickel alloy [8]. They used atmospheres of argon, air, and helium at varying pressures and ablation laser energies. It was determined that the largest aluminum peak intensities were measured in an argon amosphere; however, the lowest background plasma emission was seen for a helium atmosphere. Jensen, Langford, Dickinson, and Addleman looked at the effect of target material composition on the detection of contaminant metals in soils, quartz materials, and crystalline sand matrices [9,10]. They showed that the mass ablated per shot varies from matrix to matrix; therefore, the plasmas produced are different. It is also seen that plasma temperature varies with the matrix, and thus the amount of atomization and ionization vary. Rusak et al. presented a detailed study of the effect of water content in a sample on the laser induced plasma [11]. They showed that as the water content increased, the plasma emission decreased due to quenching, and they showed that the electron number density also decreased with increasing weight percent water. Lee et al. measured the plasma plume volume for plasmas formed by an ArF excimer laser at 193 nm on solid lead and copper targets [12]. They saw that the lead plasma was 2.5 times larger than the copper plasma. So copper, which has a high thermal conductivity and high boiling point produced

a more confined plasma with a high excitation temperature. While lead with a relatively low thermal conductivity and low boiling point created a large plasma with a lower excitation temperature.

Laser Ablation with Laser Excited Atomic Fluorescence Spectroscopy

This section will present a review of the literature showing the possibility of combining laser ablation with laser excited atomic fluorescence detection for sensitive detection of analytes in solid samples. Figure 2-3 shows a typical experimental setup for LA-LEAFS including the ablation laser, the low pressure sample chamber, a probe laser for fluorescence excitation, a monochromator, a photomultiplier tube for detection, a boxcar, and a computer.

Measures and Kwong first showed the combination of laser ablation with LEAFS in two papers which were published in 1979 [13,14]. They named their technique trace element analyzer based on laser ablation and selectively excited radiation, or TABLASER. The experimental set-up consisted of a ruby laser at 694.3 nm with an output power of 10-20 mJ which was used to create the plasma, a nitrogen laser-pumped dye laser which was used to excite the selected transition, a low pressure sample chamber, a monochromator, and a photomultiplier tube. This arrangement was used to measure chromium in National Bureau of Standards (NBS) steel, flour, and milk powder samples. They reported limits of detection on the order of 1-50 ppm. In the second paper, Measures and Kwong used the same apparatus to study possible matrix effects in the laser induced plasma. They added varying amounts of contaminants such as copper sulfate or potassium sulfate to the NBS milk powder to determine if any matrix effects would be observed. They did not see any change in the

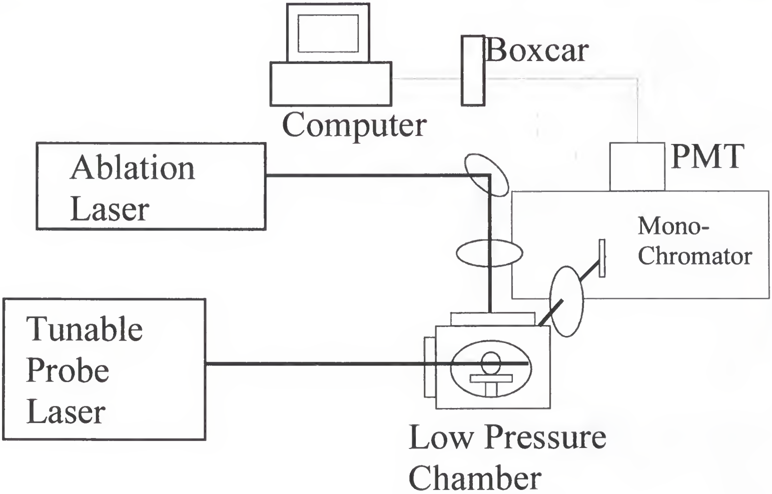

Figure 2-3: Basic experimental apparatus for LA-LEAFS.

chromium laser excited fluorescence signal from the milk powder once the contaminants had been added.

In 1983, Lewis, Beenen, Hosch, and Piepmeier demonstrated the use of LEAFS to map the regions of a laser induced plasma [15]. The experiment was comprised of two flash lamp pumped dye lasers, one was used for ablating the sample, and the second one was used for exciting the analyte atoms. A plasma was formed on the surface of a thin film containing lithium nitrate. The film was mounted inside a low pressure chamber which was connected to an x-y-z translation stage. A monochromator and photomultiplier tube were positioned perpendicular to the excitation beam in order to collect the 670.8 nm resonance fluorescence line of the lithium atoms. They were able to probe different regions of the plasma by moving the sample and thus the plasma itself with respect to the excitation laser and fluorescence collection scheme. They measured the analyte atom density in all plasma regions.

Beenen and Piepmeier used fluorescence detection to study the chemical dynamics of a laser produced vapor plume [16]. They used a dye laser to form a plasma on the surface of an aluminum alloy, and a second dye laser to excite atomic as well as molecular fluorescence inside the plasma. A monochromator and PMT were used to monitor the atomic fluorescence of aluminum as well as the molecular fluorescence of aluminum oxide. The formation of aluminum oxide was studied within all spatial and temporal regions of the plasma. The temporally resolved spatial profiles showed that the behavior of the aluminum oxide fluorescence signal was different for the peripheral and interior regions of the plasma plume. This behavior was attributed to quenching of the aluminum oxide fluorescence signals in the peripheral zones by oxygen in the surrounding atmosphere.

In 1985, Bondybey reported on the use of laser induced fluorescence to study metal dimers obtained by using a laser induced plasma [17]. This experiment was comprised of a pulsed YAG laser to create the plasma and a pulsed dye laser which was tuned to the fluorescence excitation wavelength. An adapted version of the schematic diagram of the sample chamber used in this experiment is shown in Figure 2-4. The cylindrically shaped metal sample was mounted inside a copper block, which was in thermal contact with a liquid nitrogen bath. The sample was vaporized by the pulse from the YAG laser, and the hot plasma was immediately diluted with cold helium gas. The super-cooled, dense vapor was expanded through a one millimeter orifice into the probe region of the chamber. In this region, the radiation of a pulsed dye laser passed through the vapor and excited the fluorescence transitions. The fluorescence was then collected with a monochromator and PMT. The Be_2 molecule was studied using this technique and the weakly bound ground state energy, bond length, and vibrational frequency were determined.

Fluorescence detection was used by Arlinghaus, et. al [18] to determine the speed at which zinc atoms were ejected from the surface of a ZnS crystal by laser ablation. A XeCl excimer laser at 308 nm was used to ablate the ZnS crystal, and a continuous wave narrowband dye laser was used to form the probe laser radiation. The probe laser was set to a specific delay time, t_d, with respect to the excimer laser ablation pulse. The velocity, υ, of the Zn atoms ejected from the sample surface was derived from the distance, r, which they traveled during the delay time. With a fixed delay time, the probe laser's frequency was scanned through the Doppler-shifted atomic transition of Zn. The Doppler shift is given by

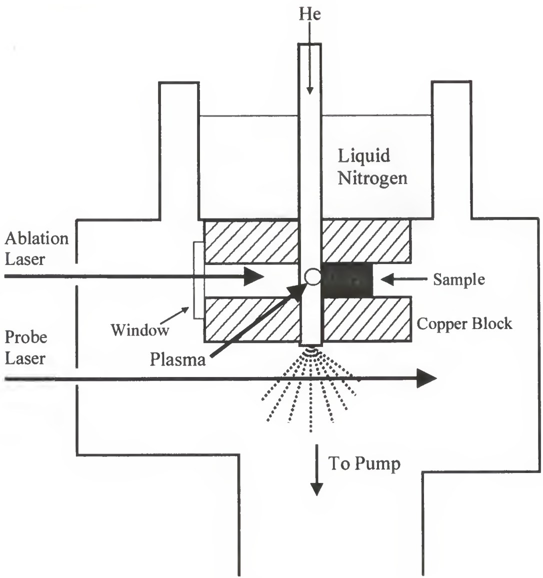

Figure 2-4: Schematic of sample chamber used to study metal dimers.

$$\nu = \nu_0(1 + \frac{r\cos\Phi}{ct_d}) \qquad (1)$$

where ν is the measured frequency, ν_0 is the frequency of the transition at zero velocity, Φ is the angle between the ablation laser propagation vector and the velocity vector of the atom, and c is the speed of light.

Sdorra, Quentmeier, and Niemax also used LA-LEAFS to study the propagation properties of the plasma plume as well as the analytical figures of merit of this technique [19]. They used the same basic experimental arrangement as described recently with a Nd:YAG ablation laser and a pulsed excimer-pumper dye laser probe beam. The laser induced fluorescence signals of chromium, boron, and silicon in the laser induced plasma produced on the surface of NBS steel samples were carefully analyzed. The fluorescence intensities of the Si 251.6 nm and 288.2 nm, the Cr 425.4 nm and 427.5 nm, and the B 249.8 nm transitions were recorded. Detection limits of 600 ng/g for Si, 10 µg/g for Cr, and 600 µg/g for B were obtained with a measurement precision of 5-8%. Taking into account the absolute mass ablated per ablation laser shot, the absolute limit of detection could be calculated. The absolute limits of detection for the two silicon transition lines were on the order of hundreds of femtograms.

In another paper, Sdorra, Quentmeier, and Niemax reported on the use of this same experimental apparatus described above to measure the collision transfer cross sections of atoms almost independently of the volatility of the elements [20]. In Figure 2-5, the partial energy level diagram of silicon is shown. When the Si transition $3s^23p^2\ ^3P_2$ - $3s^23p4s^3P_2$ at

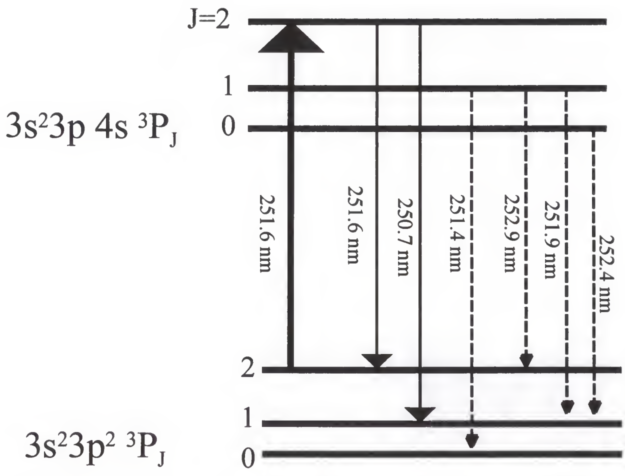

Figure 2-5: Partial energy level diagram of silicon.

251.6 nm is induced by the laser, then fluorescence occurs from the laser populated level at 251.6 nm and 250.7 nm. If the argon buffer gas atoms induce collisional transfer to other levels, then four additional lines are observed. The intensities of these lines are dependent on the argon buffer gas pressure. The fluorescence spectra reported showed that when the argon pressure was increased, the intensities of the transfer lines increased. From these spectra, the intensity ratio of transfered to directly pumped lines (I_{trans}/I_{Pump}) was obtained. This ratio is connected to the transfer rates by

$$\frac{I_{Trans}}{I_{Pump}} = \frac{A_2}{A_1}\frac{C}{D+\tau^{-1}} \qquad (2)$$

where A_1 and A_2 are the transition probabilities of the fluorescence and the transfer line respectively, and τ is the natural lifetime of the collisionally populated level. C is the transfer rate associated with the transition from the pumped to the collisionally populated fine structure level.

$$C = \bar{v}\sigma_{Trans}n_{Ar} \qquad (3)$$

D is the transfer rate associated with the depopulation of the collisonally populated fine structure level.

$$D = \bar{v}\sigma_{depop}n_{Ar} \qquad (4)$$

The average relative velocity of colliding atoms is given by $\bar{v}$, σ_{Trans} and σ_{depop} are the transfer cross-sections, and n_{Ar} is the number density of argon atoms. By taking into account

the transition probabilities of the Si lines and assuming that the transfer rates depend only on gas pressure, the fine structure transfer cross section, σ_{Trans}, was calculated.

Quentmeier, Sdorra, and Niemax also used their LA-LEAFS apparatus to evaluate a method for internal standardization of laser induced fluorescence spectroscopy in a laser induced plasma [21]. They measured the LIF signals of Si, Cr, Mn, and Mg from the laser plasma on varying metallic samples. The absolute intensities of the fluorescence signals of the elements depended heavily on the matrices of the samples. By evaluating the absolute fluorescence intensities, linear calibration curves for each element were obtained; however, the sensitivities (slopes of the calibration curves) varied among the matrices. The authors used an internal standard method for analysis by measuring the ratio of one analyte fluorescence intensity to another constituent fluorescence intensity. The relative intensities of analytes measured in different matrices will have common calibration curves if the samples are completely atomized in the plasma and if the plasma temperature is independent of the matrix. However, the plasma temperature is strongly dependent on the matrix, so the technique was not applicable to all matrices studied.

Sdorra and Niemax were also able to use LA-LEAFS to systematically measure the relative number densities of atomic and ionic species in the microplasma produced on solid samples [22]. The same experimental setup previously described was used. The relative number densities of atoms and ions were measured as functions of time and space at different argon buffer gas pressures inside the ablation chamber in order to determine the temporal and spatial distributions of the analyte atoms in the plasma. Measurements of magnesium in a copper matrix were carried out. They showed that the analyte concentration has a maximum

in the middle of the plasma. By monitoring the behavior of the ionic fluorescence, it was determined that the laser induced plasma has a hot "kernal" with an almost unchanged relative temperature distribution during a plasma lifetime up to 100 μs.

In another paper reported by Niemax and Sdorra in their series on LA-LEAFS, they reported on the analytical measurements of several elements in steel samples [23]. They showed improved detection limits and good precision in their measurements attributed to an increase in the solid angle of collection of the fluorescence signal. The doubling of the solid angle of collection was achieved by placing a concave mirror behind the plasma and reflecting fluorescence back through the plasma into the spectrograph. They reported on the analytical determinations of magnesium, boron, silicon, manganese, chromium, lead, and tin in certified steel samples obtained from the National Institute of Standards and Technology (NIST). The detection limits obtained were 0.15 to 21 ppm, which corresponded to absolute detection limits from 5-630 fg. The measurement precision improved slightly to 2-6% RSD.

In the final paper by Sdorra and Niemax on laser ablation combined with fluorescence detection, the dependence of the plasma formation on the ablation laser wavelength was considered [24]. The fourth harmonic wavelength at 266 nm as well as the fundamental wavelength at 1064 nm of a pulsed Nd:YAG laser was used for ablation of solid samples. They used different buffer gases and different samples to compare the ablated masses and plasma temperatures obtained with the two different ablation laser wavelengths. Their results suggested that poorer analytical determinations were obtained using the 266 nm radiation compared to the fundamental radiation at 1064 nm. They showed that the diameter and depth of the crater formed by the ablation laser at the fourth harmonic were larger than those of the

crater formed by the 1064 nm radiation, thus spatial resolution of the sample surface was diminished. By measuring the fluorescence intensity of silicon in the plasma and the temperature of the plasma in different regions of the laser induced plasma, it was determined that the 266 nm ablation radiation plasma was more "constricted" than the 1064 nm radiation plasma; therefore, it was concluded that the application of uv laser radiation for ablation requires an additional atomization step, for example, with an inductively coupled plasma as an additional excitation source.

Oki, Tani, Kidera, and Maeda demonstrated ultratrace analysis of impurities in water by combining laser ablation with atomic fluorescence spectroscopy [25]. The procedure used for the analysis consisted of placing a small amount of sample water, approximately 10 μL, onto a target stage which was a polished tungsten rod. The water sample was dried by a heated helium gas flow. The dried sample residue was then ablated by an excimer laser which was focused onto the target stage. After the plasma was formed, a pulsed dye laser was used to excite atomic fluorescence of sodium. The authors claimed to have achieved a detection limit of 1.7 ppt of sodium, which corresponded to an absolute detection limit of 20 fg. In a later paper by Oki, Furukawa, and Maeda using a similar experimental arrangement which differed only by the use of a continuous wave dye laser for fluorescence excitation, they reported improved detection limits for sodium [26]. Once again, they deposited 10 μL of water onto the polished tungsten surface and ablated the sample with an excimer laser. The 2σ detection limit was estimated to be 0.1 ppt or 1 fg for sodium atoms by this technique. However, they were unable to demonstrate detection of less than 1 ppt sodium due to the scatter of the resonance dye laser radiation. The log-log calibration curve reported for this

experiment had a slope of 0.3, suggesting a non-linear response over the concentration range of 1 ppt to 100 ppb. The reason for this nonlinear response was suggested to result from either the density dependence of the transportation efficiency of ablated atoms to the probe laser region or self absorption of the sodium fluorescence.

The LA-LEAFS techniques discussed so far have used resonance fluorescence as the detection scheme. Pesklak and Piepmeier demonstrated the use of nonresonance atomic fluorescence for analytical measurements in a plasma plume [27]. Nonresonance fluorescence was chosen in order to reduce the background stray light of the probe laser beam. The ablation laser was a flash lamp pumped, pulsed dye laser, and tunable pulsed dye laser with a narrowband etalon was used for the probe beam. Stainless steel samples were used in this study, and the iron content determined. By exciting ground state iron atoms with laser radiation at 296.69 nm, resonance fluorescence was observed at 296.69 nm and Stokes direct-line fluorescence was observed at 373.49 nm. The 373.49 nm transition has a larger transition rate which results in a greater fluorescence photon flux at this wavelength than that for the resonance transition. The authors used this technique to study the spatial and temporal distributions of atomic species in the plasma. The Stokes direct line fluorescence was used to detect atomic iron up to 260 μs after the ablation pulse, and the Stokes direct line fluorescence of iron resulted in a signal to noise ratio that was three times greater than for resonance fluorescence. Similar results were obtained for titanium, zirconium, and hafnium in niobium alloy samples.

Le et al. reported on laser induced fluorescence measurements of the temperature of silicon atoms and rotational temperature of SiO in a laser induced plasma produced by an ArF

excimer laser [28]. Silicon was ablated in helium, argon, and oxygen atmospheres in order to understand the formation of molecules and clusters. Thermal relaxation processes of atomic silicon in He and Ar atmospheres were studied by measuring the Doppler profile of the Si line using the transition centered at 263.128 nm, and the thermalization of Si was determined to occur much faster in a He atmosphere than in an Ar atmosphere. No evidence of the nonequilibrium of the rotational and vibrational modes was observed, and the LIF measurements indicated that the formation of SiO molecules was better described by a gas phase equilibrium reaction in the temperature range of 400-2000 K.

Time resolved planar laser induced fluorescence was used to image copper in a laser induced plasma plume by Zerkle and Sappey [29]. A dye laser was focused onto a solid copper target in order to generate the plasma, and the copper fluorescence was excited with a second pulsed dye laser. The purpose of this work was to determine the ground state copper atom number density in dense condensing laser ablated copper plasmas. The atom number density could then be used to determine values for the condensation reaction rate coefficients that govern copper cluster growth. The condensation rates were found to be different for different test volumes within the plume. The region of highest copper atom density quickly formed Cu_2 and some larger copper clusters. These clusters collected more copper atoms, and so the region that once possessed the greatest number of copper atoms eventually possessed the least number.

Neuhauser et al. used laser plasma spectroscopy and laser excited atomic fluorescence to detect lead in aerosols [30]. Lead nitrate aerosols with particle diameters between 10 and 300 nm were generated by ultrasonic nebulization of aqueous lead nitrate solutions.

Atomization of the aerosol particles was achieved by creating a laser induced plasma with a Nd:YAG laser, and the atomic fluorescence was excited with a dye laser tuned to the 283 nm resonance transition of lead. A correlation between the detection limit and the particle diameter was discovered. The detection limit increased from 55 ng m^{-3} for a particle diameter of 48 nm to 130 ng m^{-3} for a particle diameter of 300 nm. The increasing detection limit with increasing particle diameter was attributed to the incomplete atomization of larger particles in the colder periphery of the plasma.

Oki, Matsunaga, Nomura, and Maeda demonstated the possibility of determining the depth distribution of an element with subnanometer resolution by applying LA-LEAFS [31]. An ArF excimer laser at 193 nm was used to create a plasma which removed a thin surface layer from a solid glass sample on the order of 1.1 nm/shot for the first 50 shots and 0.4 nm/shot after that. By monitoring the LIF signal of the Na atoms removed with each shot, the depth distribution of sodium was determined.

The concentrations of lead in the range of 0.15 - 750 μg/g were measured in metallic matrices of copper, brass, steel, and zinc by LA-LEAFS by Gornushkin, Baker, Smith, and Winefordner [32]. An excimer laser was used for ablation, a dye laser was tuned to the lead 283 nm line, and the fluorescence was collected at 405.8 nm. No matrix effects were observed, so that a universal calibration curve for all samples was used with a relative standard deviation of 20%. The relative and absolute limits of detection were 72 ng/g and 0.5 fg of lead, respectively.

Laser Ablation with Atomic Absorption Spectroscopy

Conventional methods for atomic absorption spectroscopy such as graphite furnace atomic absorption, flame atomic absorption, and inductively coupled plasma atomic absorption, require the samples to be in the form of a liquid for introduction. So it is often necessary to use a digestion or dissolution procedure in order to prepare solid samples for analysis, and a method which allowed direct sampling of solids would be attractive. Laser ablation or laser induced plasma techniques have shown the capability for direct analysis of solids; however, intense self-reversed emission is sometimes seen in LIP-OES. It should be considered that atomic absorption would be a better method for measuring some analyte concentrations in a laser induced plasma than atomic emission is. This section gives a review of the few experiments which have combined AAS detection with laser induced plasmas.

In 1993 Darke and Tyson published an extensive review of the literature on laser ablation of solid materials and its significance to analytical spectrometry [33]. They showed schematics for the possible configurations for measuring atomic absorption of laser ablated materials. Different arrangements including measuring the absorption directly through the plasma itself or transferring the ablated material via a gas flow into a further excitation source. A representation of these experimental procedures are given in Figures 2-6 through 2-9.

Atomic absorption detection in a laser induced plasma was first demonstrated by Mossotti, Laqua, and Hagenah in 1967 [34]. Their basic experimental setup is of the type shown in Figure 2-6. The radiation output of a ruby laser was focused onto the surface of the target material to form a plasma. A low-pressure xenon flash lamp was used as the radiation source for the atomic absorption system. Off-axis multiple pass optics, shown schematically

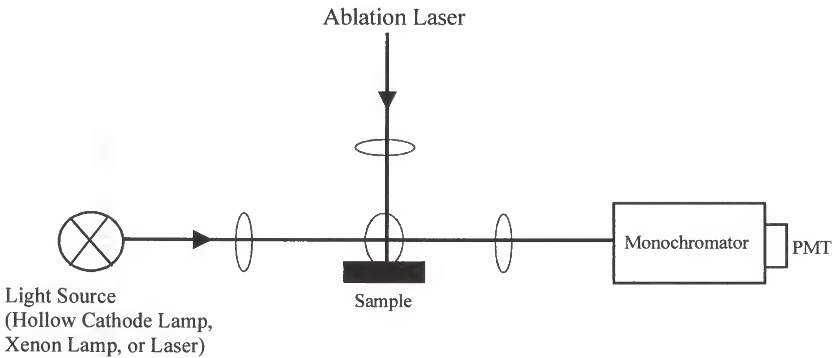

Figure 2-6: Configuration for measuring AAS directly in a plasma.

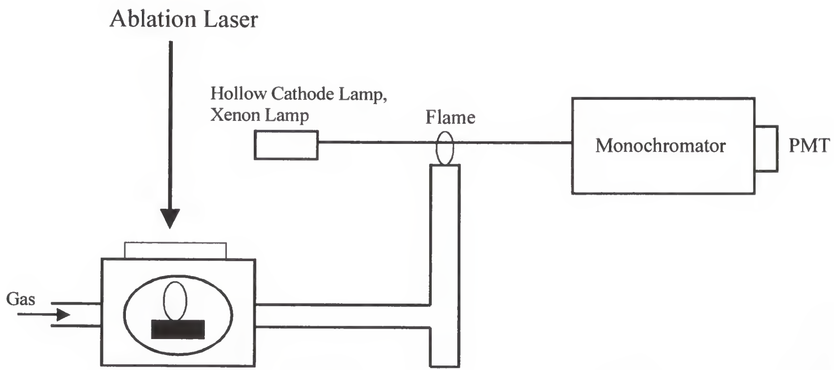

Figure 2-7: Configuration for measuring AAS of material ablated from a solid sample.

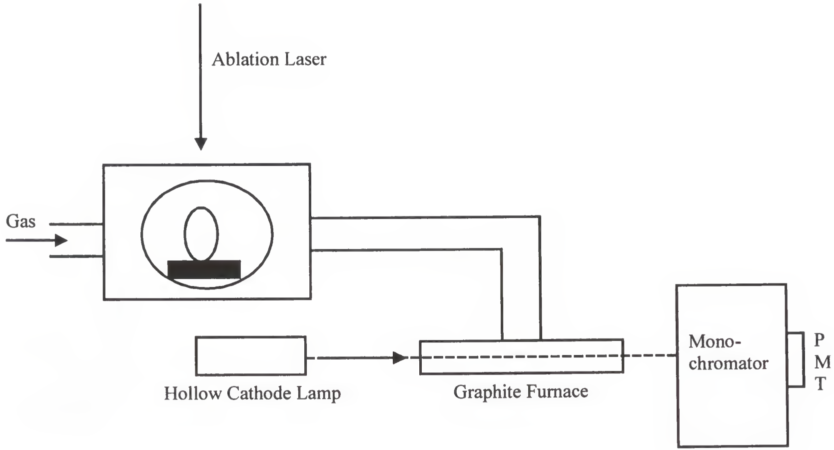

Figure 2-8: Configuration for measuring AAS of material ablated from a solid sample in a graphite furnance.

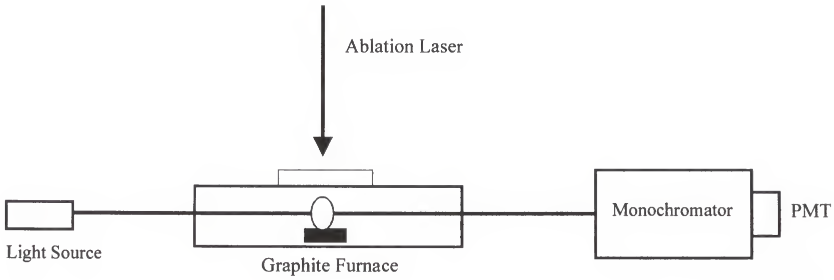

Figure 2-9: Configuration for measuring AAS of a solid sample directly in a graphite furnace.

in Figure 2-10, were used to increase the absorption path length by increasing the number of passes through the plasma. A monochromator was used to isolate the atomic absorption line from the continuum background plasma emission. Using this arrangement, the authors were able to measure the atomic absorption of copper, silver, and calcium in graphite at concentration ranges of 0.003-0.1 weight percent.

A decade later, Ishizuka, Uwamino, and Sunahara used a ruby laser to vaporize small amounts of solid samples and then swept the vapor into an absorption cell [35]. They were able to measure the atomic absorption in the cell by using hollow cathode lamps and a photomultiplier tube. The solid sample was placed inside an ablation chamber, and the ruby laser radiation was focused onto the surface of the sample. The atomic vapor which was produced was swept into a quartz cell by the flow of argon gas. The absorption signals of aluminum, chromium, copper, iron, manganese, molybdenum, nickel, and vanadium were measured from brass, steel, and aluminum alloys. Detection limits on the order of tens of parts-per-millions with measurement precisions ranging from 1-12 % were obtained.

In a series of papers, Quentmeier, Laqua, and Hagenah demonstrated the use of AAS to measure microgram amounts of copper, manganese, magnesium, iron, zinc, and silicon in aluminum samples. They used a Nd:YAG laser to form the plasma and a continuum lamp and monochromator and PMT to measure the absorption. They reported detection limits of approximately one ppm for the elements Cu, Mn, and Mg. They also reported on the temporal and spatial development of the plasma plume by mapping the absorption of the atomic species in the different regions of the plasma [36,37].

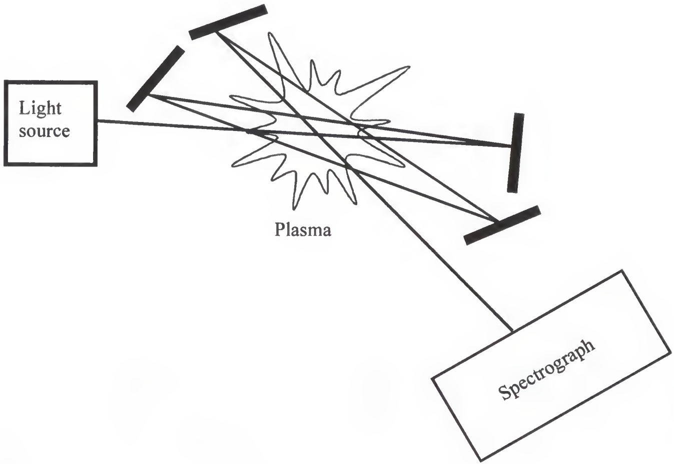

Figure 2-10: Multi-pass optical system for atomic absorption measurements in a laser induced plasma.

Manabe and Piepmeier reported on temporally and spatially resolved atomic absorption measurements made using a pulsed dye laser to atomize solid steel and graphite samples and using pulsed hollow cathode lamps as the primary sources for the AAS measurements [38]. Using the relatively noisy pulsed hollow cathode lamps, they obtained measurement precisions on the order of 10-20%. While the authors reported extensively on the temporal profile of the AAS signals obtained, no analytical measurements were performed.

Sumino et al. reported on the use of LA-AAS for the analysis of cadmium in human kidney tissue [39]. A Nd:YAG laser was used to ablate microamounts of the tissue, and a cadmium hollow cathode lamp was used as the source for absorption measurements. While the majority of this paper discussed the sample preparation for the biological specimens, they reported some analytical information. Kidney specimens from three different autopsy cases which had known concentrations of cadmium by previous measurement were used to construct a calibration curve. A fourth kidney specimen was used as an unknown, and its cadmium concentration was found to be 45 ± 8 ppm. Acid digestion of the unknown sample showed that the kidney had 43 ppm cadmium.

The simultaneous determinations of Ag-Mn and Pb-Ag by laser ablation atomic absorption spectroscopy was reported by Wennrich and Dittrich [40]. A Q-switched ruby laser was used to ablate microamounts of a copper target, and the vapor plume was swept into a hot graphite furnace by an argon gas flow. Hollow cathode lamps were used as the AAS source, and two monochromators and PMTs were used as detectors. They reported detection limits from 5-100 ppm in the copper matrix which corresponded to absolute

detection limits in the picogram range. They were able to demonstrate comparable figures of merit to flame AAS, which indicated the potential for using LA-AAS with a graphite furnace for analysis of solid samples without first having to dissolve the sample.

Harnafi and Dubreuil used a laser induced plasma to vaporize a copper target in order to measure the lithium atomic absorption [41]. They used a pulsed CO_2 laser to induce the plasma, and a N_2 laser-pumped dye laser for probing the 670 nm transition in lithium. When a laser is used to excite the absorption transition, absorption saturation can become a factor. This occurs when the rate of absorption by the atoms is equal to the rate of stimulated emission induced by the high energy density laser. If this occurs, no change in radiation intensity is seen by the detector; therefore, no net absorption is recorded. The authors reported that they kept the dye laser beam intensity low enough to avoid saturation effects. Using the dye laser to probe successive plasma heights, they were able to determine the velocity at which the Li atoms were ejected from the surface. For a laser energy of 0.9 J/cm^2, approximately 5 x 10^{11} atoms were emitted per ablation laser shot with a center-of-mass velocity of 3 x 10^5 cm/s and a plasma temperature of 8500-10,000 K.

Tanaka et al. used frequency quadrupled radiation at 266 nm from a Nd:YAG laser to form a laser induced plasma on solid NiO pellets [42]. A xenon flash lamp was used as the primary source for absorption measurements in the plasma. The ablated species in different electronic states such as the ground state, low-lying states, and excited states were studied. Using an ablation laser fluence of 5.1 J/cm^2, they determined that Ni^+ ions move faster than Ni neutrals by measuring the appropriate velocities. This is due to the fact that the Ni^+ ions were further accelerated by the electric field within the center portion of the plume. It is

concluded that most of the species are initially ejected as NiO molecules or clusters, and then dissociated into Ni and O species in the plasma plume.

Isotope Analysis

Isotope analysis is important for many fields of study including geology, medicine, and the nuclear science industry. Historically, the measurement of isotopes has been dominated by mass spectrometric techniques. These techniques are very accurate and precise, but they are expensive and require sample dissolution steps for solid samples before analysis. Isotopes have been measured spectroscopically, but these methods tend to have poorer precision and higher detection limits. Also, only certain elements (either low mass or high mass elements) exhibit an isotope shift large enough to measure spectroscopically.

Uranium has a relatively large isotope shift, and this shift was measured by Goleb using an atomic absorption technique [43]. The ^{235}U / ^{238}U isotope ratio was measured inside a water-cooled hollow cathode discharge tube. Wheat demonstrated the isotopic resolution of ^{6}Li and ^{7}Li in a flame using monoisotopic hollow cathode lamps [44], and Meier was able to determine the ^{6}Li and ^{7}Li concentrations in real geological samples using a similar apparatus [45]. While uranium and lithium isotopes could be measured by these early techniques, significant deconvolution of the peaks had to be employed.

With the development of narrowband lasers, such as the diode laser, laser source atomic absorption (LAAS) became a viable technique for spectroscopically measuring isotopes. These narrowband sources opened the door to studying many other elements which do not have as large an isotope shift as lithium and uranium. Because of suitable wavelengths,

rubidium isotopes have been studied by several groups using diode lasers. Gibbs and Churchill used a diode laser to probe a rubidium atomic beam in order to determine the isotope shift of the D1, 794 nm, line of rubidium [46]. They were able to determine that the ^{87}Rb absorption spectrum was shifted by 77 ± 3 MHz relative to the ^{85}Rb absorption spectrum. Gustafson, Rojas, and Axner were able to see the isotope shift of the rubidium D2 transition at 780 nm in a graphite furnace at low pressure using diode lasers [47]. Song et al. were able to use a narrowband diode laser to determine the structure of the rubidium D1 and D2 transitions in a hollow cathode glow discharge cell [48]. They reported spectra showing not only the isotope structure but the hyperfine components as well.

Much work has been done by Niemax and coworkers on using Doppler-free laser spectroscopy techniques to resolve isotopes. They have published several papers discussing the potential and applicability of this technique. Using Doppler-free two photon laser enhanced ionization, they were able to resolve the isotopes of calcium [49]. In an extensive review of diode laser spectroscopy, they show isotope resolution for rubidium and lithium in a graphite furnace with Doppler-free absorption techniques [50]. Recently, Wizeman and Niemax reported on the isotope selective elemental analysis by diode laser atomic absorption of rubidium and lithium in a graphite furnace with improved detection limits and precision [51]. They were able to construct linear calibration curves from the standard Rb and Li solutions, and they obtained detection limits of 0.2 ng/mL and 0.45 ng/mL for ^{85}Rb and ^{87}Rb respectively. These values correspond to an absolute detection limit of 1.4 pg for ^{85}Rb and 1.3 pg for ^{87}Rb. Similar results were obtained for lithium, with detection limits of 0.22 ng/mL for ^{7}Li and 0.55 ng/mL for ^{6}Li. These authors were also able to demonstrate the usefulness

of isotope dilution for the cancellation of matrix effects and for calibration. They also used isotope dilution of lead to study the ^{206}Pb, ^{207}Pb, and ^{208}Pb isotope shifts [52].

Only very recently has it been realized that isotope structure could be observed in a laser induced plasma. This is a surprising observation because of the high temperature and high electron number density characteristics of the laser plasma which are expected to result in significant line broadening and the overlap of isotope structure. At the time the work presented in this dissertation was begun, no one had yet published results showing the potential of isotope analysis in a laser induced plasma. However, recently, Niki, Yasuda, and Kitazima were able to measure the isotope ratio of ^{10}B / ^{11}B in a plasma by observing the shifts of the emission bands from the ^{10}BO and ^{11}BO molecules [53]. Pretsch, Petit, and Briand determined the isotope ratio of ^{235}U and ^{238}U in natural and enriched uranium samples by LIP-OES. The isotope shift for U is 25 pm; therefore, some peak deconvolution was necessary in the emission spectra [54]. Smith and coworkers were able to use LA-LEAFS to resolve the uranium isotopes in a laser induced plasma formed on the surface of a natural uranium sample at low pressure using a diode laser to excite the 682.7 nm resonance fluorescence transition [55].

One important field for isotope analysis is in geochemistry. Geological systems are dated by using atomic clock systems which are based on the decay of isotopes. Some examples of these dating systems are the Pb-Pb system [56,57,58], the ^{10}Be-^{9}Be system [59], the Kr-Ar system [60], and the Rb-Sr system [61]. The Rb-Sr atomic clock is a simple age determination method based on the decay of ^{87}Rb to ^{87}Sr, so a rock which is found today has a total ^{87}Sr concentration which is the sum of the original ^{87}Sr and the ^{87}Sr which was formed

by decay of ^{87}Rb. Therefore,

$$^{87}Sr = Sr_0 + {}^{87}Rb(e^{\lambda t} - 1) \qquad (5)$$

where λ is the decay constant based on the half life of ^{87}Rb, and t is the time in years. Since it is much easier to measure isotope ratios than it is to measure absolute atom number densities, the above equation can be divided through by the concentration of ^{86}Sr which is a stable atom, thus its concentration is considered unchanged.

$$\frac{^{87}Sr}{^{86}Sr} = \left(\frac{^{87}Sr}{^{86}Sr}\right)_0 + \frac{^{87}Rb}{^{86}Sr}(e^{\lambda t} - 1) \qquad (6)$$

This equation has the form of a line, and an isochron can be constructed. An isochron is a plot of the ^{87}Rb / ^{86}Sr ratio versus the ^{87}Sr / ^{86}Sr ratio. If a number of types of rocks, for example basalts, quartzes, lava rocks, limestones, etc., is obtained from a given geological formation or region, then these different types will all have different concentrations of rubidium and strontium. Therefore, the isotope abundance ratios will be different for each sample, and the isochron for the system can be constructed as in Figure 2-11. The slope of the isochron is given by ($e^{\lambda t}$-1), and since λ is known for any given element, the age or time of the system, t, can easily be determined. [62].

Another important application of isotope analysis is in high level nuclear wastes [63,64,65]. The main components of nuclear waste are fission products. These are present due to the spontaneous fission of heavy atoms such as ^{235}U. The steps of the spontaneous fission process are illustrated in Figure 2-12. First, the nucleus oscillates from a spherical

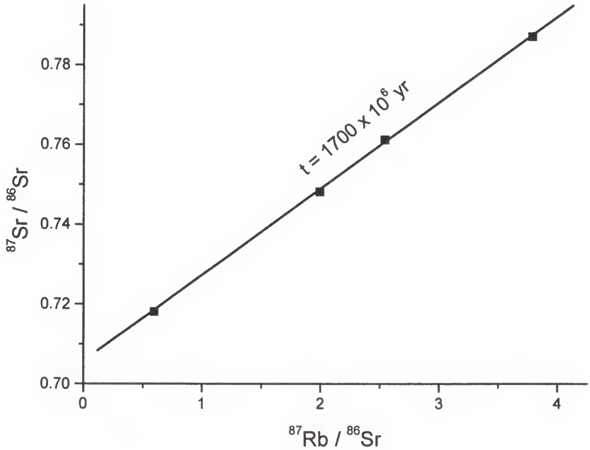

Figure 2-11: Simulated isochron for the Rb-Sr dating method.

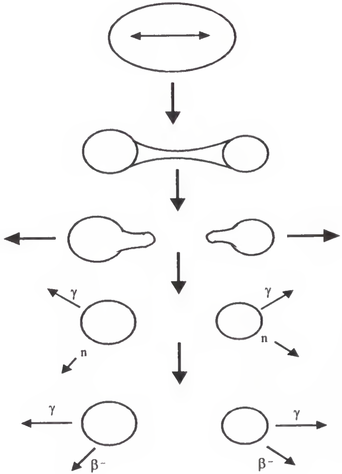

Figure 2-12: The steps of spontaneous fission.

shape into a more and more ellipsoidal shape, until it attains the shape of a dumbbell. Then the nucleus splits into two parts. The two parts formed are of different mass but similar excitation energies. The coulomb repulsion energy, which is greater than the nuclear forces, drives the products apart, and the fission products attain high kinetic energies. The highly excited fission products emit neutrons and protons. All of these processes occur within 10^{-15} s. The fission products then undergo beta-minus emission or γ-ray photon emission in order to reach a stable nuclear configuration. Since two fission products are formed from each ^{235}U nucleus, the total mass yield must total 200%. A mass yield curve for ^{235}U is shown in Figure 2-13, which indicates that 2.55% of the ^{235}U fissions will yield mass 87, and 1.32% of the fissions yield mass 85. This gives an abundance ratio of approximately 2:1 for the 87 / 85 ratio. However, the natural abundance ratio of ^{87}Rb / ^{85}Rb is 27.8% / 72.2%, or 1:2.6. The ratios of the fission yield products change over time due to the decay process until a stable nucleus is obtained; therefore, the isotope abundances can give useful information of the properties and lifetimes of the waste [66,67]. A method for rapidly identifying and measuring isotope ratios without handling of the sample would be beneficial to monitoring of radioactive waste.

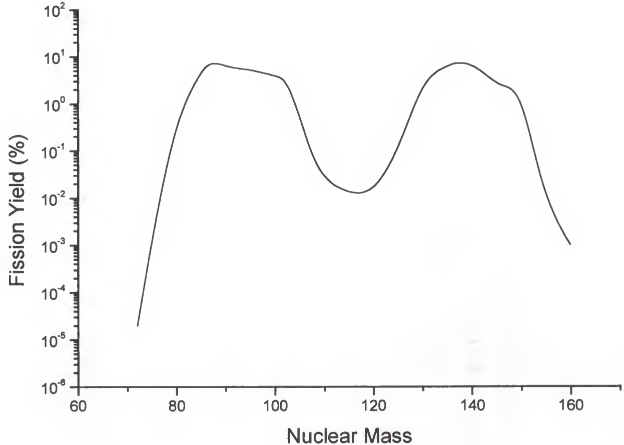

Figure 2-13: Fission yield curve for Uranium-235.

CHAPTER 3
THEORETICAL PRINCIPLES OF ISOTOPE SHIFTS AND ISOTOPE ANALYSIS

Isotope Shift

Very small differences in the spectra of isotopes can be observed. These differences in corresponding electronic states of the isotopes of a given element are called isotope shifts. For light elements, this shift is caused by a large relative difference in the nuclear mass of the isotopes and is called the mass effect. However, this effect decreases rapidly with increasing atomic weight, so the isotope shift which is observed in heavier elements must be due to a different phenomenon. The reason for the isotope shift in heavier elements is the volume effect. The volume or field- effect occurs because of the different charge distributions in the nuclei of the isotopes.

Mass Effect

The solution to the Schrödinger equation for a hydrogen like system gives the possible energies for electronic states of principle quantum number n as [68]

$$E_n = -\frac{Z^2 \mu e^4}{32\pi^2 \varepsilon_0^2 h^2} \frac{1}{n^2} \qquad (7)$$

where μ is the reduced mass, mM/(m+M), m is the mass of the electron, M is the mass of the nucleus, ϵ_0 is the permittivity of free space, e is the electron charge, h is plank's constant, and

Z is the nuclear charge. If this equation is differentiated with respect to M and divided by E in order to eliminate the constant terms, then the shift $\Delta\sigma$ in a line of wavenumber σ for two atoms with nuclear masses M_1 and M_2 differing in mass by ΔM is given by the following equation [69].

$$\frac{\Delta E}{E} = \frac{\Delta \sigma}{\sigma} = \frac{\Delta \mu}{\mu} = \frac{m \Delta M}{M_1 M_2} \qquad (8)$$

It is easily seen that the energy level shift is proportional to the relative mass difference. However, as the mass, M, increases the isotope shift decreases so this effect is not observed in heaver elements, specifically those with atomic number ≥ 30.

Volume Effect

Pauli and Peierls [70] first suggested that the isotope shifts observed in the heavier elements (atomic number ≥ 50) is caused by the finite size or volume of the nucleus. The nuclear charge distribution is altered by the addition of neutrons to the nucleus. When the size and shape of the nuclear charge distribution is altered for different isotopes, the electrostatic interaction with any electron charge distribution which overlaps the nuclear charge distribution is also perturbed. This is the case for s-electrons and sometimes p-electrons which have a reasonable probability of being located near the nucleus [71]. The isotopic shift due to the volume effect increases as the mass of the nucleus increases, so isotope shifts of approximately a wavenumber are reported for the heaviest elements [69].

Isotopes and Laser Excited Atomic Fluorescence Spectroscopy

A two-level atomic scheme is shown in Figure 3-1. For atomic fluorescence, the absorption rate $B_{ij}\rho_\upsilon n_i$ generally exceeds the collisional excitation rate $k_j n_i$, so the strength of an atomic fluorescence line is directly proportional to the absorbed radiant power, Φ_A (W). The total fluorescence power is also dependent on the fluorescence quantum efficiency, Y, which is defined as the rate constant for spontaneous emission divided by the sum of the rate constants for all of the other possible deexicitation pathways. Therefore, the total fluorescence radiant power, Φ_{FL} is the product of the absorbed radiant power and the fluorescence quantum efficiency.

$$\Phi_{FL} = \Phi_A Y \qquad (9)$$

If the source used to excite the fluorescence is a line source that emits at λ_m (m), then the absorption radiant power is given by

$$\Phi_A = \Phi_0 \alpha_L \qquad (10)$$

where α_L (dimensionless) is the absorption factor for the line source, and Φ_0 is the incident source radiant power. When optically thin conditions are considered, α_L is given as

$$\alpha_L = \frac{e^2 \lambda_m{}^2 n_i f_{ij}}{4\varepsilon_0 m_e c^2 \Delta\lambda_{eff}} l \qquad (11)$$

where e is the electron charge (C), n_i is the population of level i, f_{ij} is the oscillator strength for the transition from level i to level j, and $\Delta\lambda_{eff}$ is the effective width of the line profile, m_e is the mass of the electron (kg), c is the speed of light (m s^{-1}), ϵ_0 is the permittivity of free

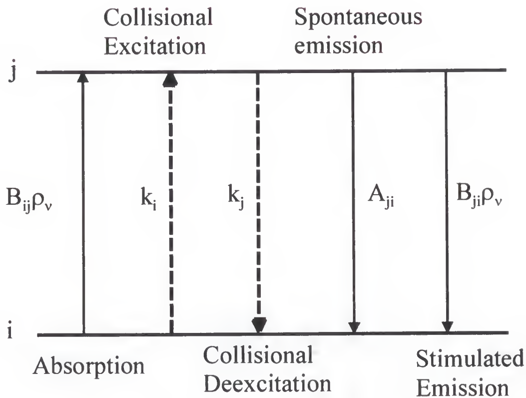

Figure 3-1: Two-level atomic scheme. The rate constants for each process are given in the diagram. B_{ij} and B_{ji} are the Einstein coefficients for stimulated absorption and stimulated emission, respectively. The radiation field energy density at a frequency ν is ρ_ν. A_{ji} is the Einstein coefficient for spontaneous emission.

space ($C^2 N^{-1} m^{-2}$), and l is the absorption path length (m). Manipulating equations 9, 10, and 11 gives the expression for the fluorescence radiant power.

$$\Phi_{FL} = \frac{e^2 \lambda_m^{\ 2} \Phi_0 Y l f_{ij} n_i}{4\varepsilon_0 m_e c^2 \Delta\lambda_{eff}} \qquad (12)$$

The oscillator strength, f_{ij}, describes the number of electrons per atom undergoing a radiative transition, and it is related to the transition probability, the level degeneracy, g, and Einstein coefficients, A_{ji}, by the following equation.

$$f_{ij} = \frac{A_{ji} \lambda_m^{\ 2} \varepsilon_0 m_e c g_j}{2 g_i \pi e^2} \qquad (13)$$

It is seen that the oscillator strength is related to the ratio of the level degeneracies. The g-values are determined from the quantum number J [72, 73].

$$g = 2J + 1 \qquad (14)$$

In the case of analyzing the lithium isotopes by fluorescence, the two lines which are evaluated are the transition $2S_{1/2} \rightarrow 2P_{1/2}$ for ^6Li, and the transition $2S_{1/2} \rightarrow 2P_{3/2}$ for ^7Li. Substituting the relevant g-values into the fluorescence power equation, the expressions for each lithium isotope can be determined.

$$^6Li: \qquad \Phi_{FL} \propto n_i \frac{g_j}{g_i} \propto n_i \frac{2}{2} \propto n_i \qquad (15)$$

$$^{7}Li: \qquad \Phi_{FL} \propto n_i \frac{g_j}{g_i} \propto n_i \frac{4}{2} \propto 2n_i \qquad (16)$$

Therefore, the ratio of the fluorescence intensities must be corrected by a factor of two in order to obtain the true isotope ratio of ^{7}Li / ^{6} Li.

The use of a laser source in atomic fluorescence spectroscopy offers several advantages, including the ability to saturate the atomic transition because of the high spectral energy density of the laser. It can be seen from equation 12 that as the incident source radiant power, Φ_0, increases, so does the fluorescence intensity, Φ_{FL}. However, even though the fluorescence signal saturates at increasing laser power, the resonance fluorescence scattering signal does not. Therefore, the interference from the scattering signal worsens as the laser power is increased, so an optimum laser power must be used. This optimum power is determined from a plot of Φ_{FL} as a function of Φ_0, which is called a saturation curve. The saturation curve asymptotically approaches a plateau value as $\Phi_0 \rightarrow \infty$ [72].

Isotopes and Laser Atomic Absorption Spectroscopy

If we consider an absorbing medium with a uniform concentration and a monochromatic source, then an expression for the amount of radiation absorbed by the medium can be determined. The source radiant power incident on a thin slice of the absorbing medium is Φ, and the amount of radiation absorbed is $d\Phi$. Since the number of absorbing species which interact with the beam is directly proportional to the thickness of the slice, dl, the amount of radiation absorbed can be expressed as [73]

$$d\Phi = -k\Phi\, dl \qquad (17)$$

where k is the absorption coefficient (cm^{-1}) which is dependent on wavelength and concentration, and the minus sign indicates the attenuation of the incident radiation. The absorption for an absorbing medium of finite thickness l , where Φ_0 is the incident radiant power at thickness zero and Φ is the radiant power emerging at thickness l, is easily determined.

$$\int_{\Phi_0}^{\Phi} \frac{d\Phi}{\Phi} = -k \int_0^l dl \qquad (18)$$

This equation can be expressed as

$$\ln \frac{\Phi}{\Phi_0} = -kl \qquad (19)$$

or

$$\Phi = \Phi_0 e^{-kl} \qquad (20)$$

which indicates that the transmitted radiant power decreases exponentially with increasing distance through the absorbing medium. The transmittance $T = \Phi/\Phi_0 = e^{-kl}$ is most often the quantity measured in absorption spectroscopy. The absorbance is defined as $A = -\log T = kl$. Absorbance is a linear function of the concentration dependent term k. This expression is commonly referred to as the Beer-Lambert Law.

For atomic absorption, the case of a narrow spectral line source can be considered to determine the relationship between absorbance, A, and the number of analyte atoms n_i. When

the spectral profile of the source is much narrower than that of the absorption coefficient, $k(\lambda)$ can be considered constant over the source profile and equal to its maximum value, k_m. Therefore, the absorption factor for a line source is given by [73]

$$\alpha_L = \frac{(\Phi_\lambda)_0 - \Phi_\lambda}{(\Phi_\lambda)_0} \qquad (21)$$

and if Beer's law for the wavelength dependent spectral radiant power is substituted into the above expression, then α_L is given by the following.

$$\alpha_L = \frac{\int (\Phi_\lambda)_0 (1 - e^{-k_m l}) d\lambda}{\int (\Phi_\lambda)_0 d\lambda} = 1 - e^{-k_m l} \qquad (22)$$

The absorption coefficient k_m is dependent on wavelength and concentration by [72]

$$k_m = \frac{e^2 \lambda_m{}^2 n_i f_{ij}}{4\varepsilon_0 m_e c^2 \Delta\lambda_{eff}} \qquad (23)$$

and the peak absorbance, A_L, is given by A_L=-log(1-α_L)=0.434k_ml. Therefore, if the absorbance value is measured at the peak absorbance, then the absorbance is directly proportional to the atom number density, n_i. [73].

$$A_L = 0.434 \frac{e^2 \lambda_m{}^2 n_i f_{ij} l}{4\varepsilon_0 m_e c^2 \Delta\lambda_{eff}} \qquad (24)$$

CHAPTER 4
ANALYSIS OF RUBIDIUM AND POTASSIUM IN SOLIDS

Introduction

The original goal of this project was to evaluate the possibility of using laser excited atomic fluorescence and laser source atomic absorption as detection schemes for laser induced plasma spectroscopy. Typically, optical emission is detected for identification and quantification of the species in a laser induced plasma. However, fluorescence and absorption can provide more sensitivity than emission. In these experiments, the fluorescence and absorption of rubidium and potassium have been measured with good sensitivity, precision, and accuracy in several solid matrices.

Experimental

The experimental arrangement is shown in Figure 4-1. A Nd:YAG laser at the fundamental wavelength of 1064 nm was focused onto the surface of a solid sample. For the rubidium measurements a Laser Photonics Nd:YAG was used, and for the potassium measurements a Quantel Nd:YAG laser was used for ablation. The samples used were solid pressed pellets of copper or NIST standard reference materials. The samples were placed inside a 6 cm x 6 cm x 6 cm stainless steel chamber with quartz windows on five sides of the chamber. The excitation beam was provided by a Ti:Sapphire laser (Schwartz Electro

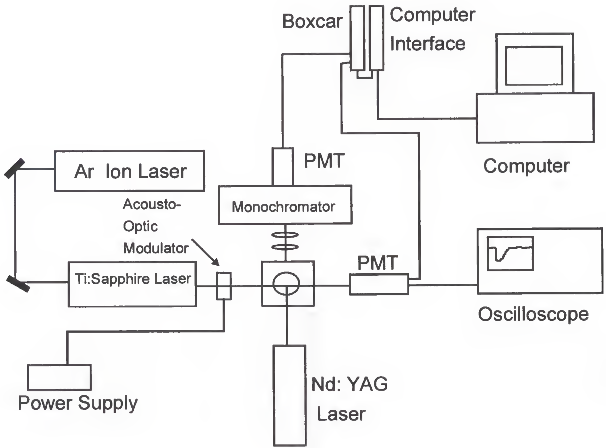

Figure 4-1: Experimental apparatus for detecting atomic fluorescence and atomic absorption in a laser induced plasma.

Optics, Titan series, USA) which was pumped by a 5.0 W argon ion laser (model # 2060, Spectra Physics, USA). The Ti:Sapphire laser was operated in the ring mode such that the bandwidth was 400 MHz.

The resonance atomic fluorescence which was excited in the plasma was collected at ninety degrees to the excitation beam by a monochromator (Digikrom 240, CVI, USA) and a red-sensitive PMT (R363, Hamamatsu, Japan). A boxcar (Stanford Research Systems, SR250, USA) was used to integrate the fluorescent signal with a gate width of 300 μs and a delay time set to zero, such that the initial 300 μs of fluorescence signal was collected. The fluorescent signal was measured for an argon atmosphere pressure of 1.0 Torr.

A second PMT was positioned behind the sample chamber in line with the excitation beam in order to monitor the absorption of the Ti:Sapphire radiation by the analyte atoms in the plasma. Another boxcar was used to collect the absorption signal and the gate width and delay time were set to 5 μs and 100 μs respectively. The atomic absorption was also measured at an argon pressure of 1.0 Torr. The PMT signal for the probe radiation with no plasma was recorded for the initial intensity (I_0), and the amount of light passing through the plasma was recorded as the signal (I), so that the total fraction of light transmitted (I/I_0) could be determined. This fraction is T, and absorbance, A, is easily calculated from Beer's law, $A = -\log (T)$.

The samples used in this experiment were all fine powders which were pressed into solid pellets. The copper matrix standards were prepared by depositing an aqueous RbCl or KCl solution into the fine copper powder, mixing well, drying, and pressing into solid samples with a hydraulic press.

Results and Discussion

Partial energy level diagrams illustrating the probed transitions are given in Figure 4-2. The resonance fluorescence of rubidium at 780 nm was measured in copper samples. Optical saturation of fluorescence was checked to insure that saturation conditions were met in order to obtain the best possible fluorescence signal. This is shown in Figure 4-3. Working at a Ti:Sapphire power of 200 mW, which corresponds to the optimum fluorescence excitation power, copper standards with rubidium concentrations from 1-1000 ppm were analyzed. The resulting calibration curve was linear with measurement precisions of 5-10% RSD. (Figure 4-4) The 3σ limit of detection was determined to be 580 ppb. By measuring the average mass ablated per laser shot, the absolute limit of detection was calculated. For rubidium, this was determined to be 350 fg.

The 766 nm resonance fluorescence of potassium was measured in prepared copper samples. The calibration curve for potassium is given in Figure 4-5. The fluorescence intensity is linear with concentration, and the measurement precision is 10-20% The precision is worse for potassium than for rubidium because of the different Nd:YAG ablation laser used, the Quantel Nd:YAG was significantly older and required the use of several prisms for steering the beam to the chamber, so the shot-to-shot reproducibility was 10% at the experiment. This was significantly worse than the 5% shot-to-shot reproducibility of the Laser Photonics Nd:YAG laser. The 3σ limit of detection was found to be 200 ppb with a corresponding absolute limit of detection of 50 fg.

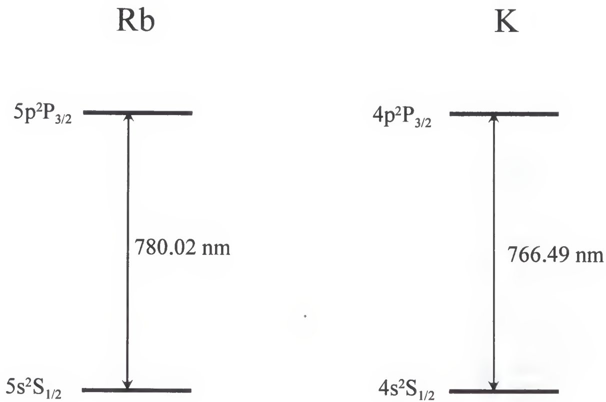

Figure 4-2: Partial energy level diagrams of rubidium and potassium as adapted from Radzig and S,irnov [74].

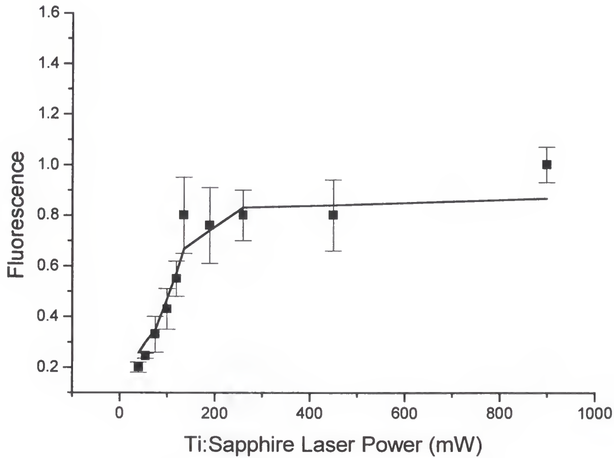

Figure 4-3: Fluorescence saturation curve of rubidium.

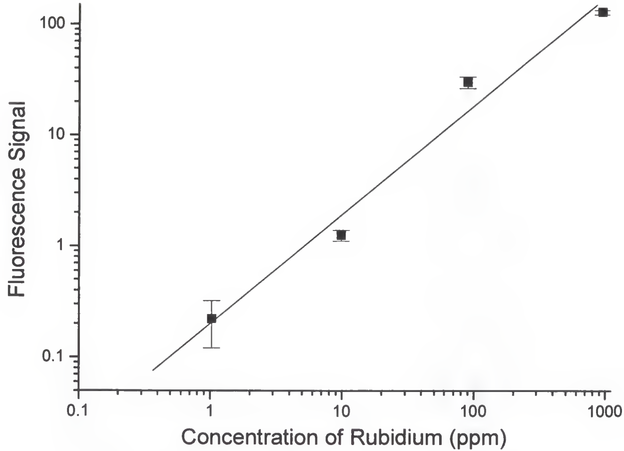

Figure 4-4: Fluorescence calibration curve of rubidium in a copper matrix.

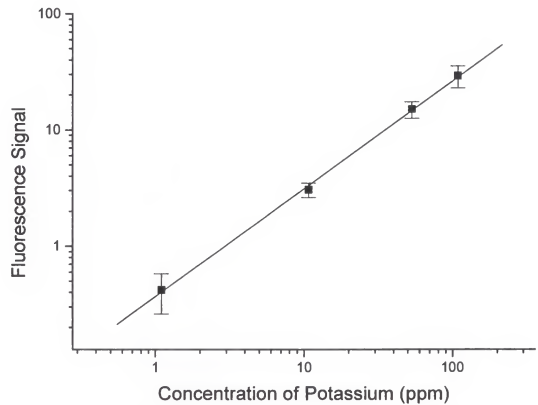

Figure 4-5: Fluorescence calibration curve for potassium in a copper matrix.

The accuracy of this technique was evaluated by analyzing the potassium fluorescence signals from NIST standard reference materials (SRM). Three iron ore samples were available, and SRM 690 (K concentration of 25 ppm) and SRM 692 (K concentration of 320 ppm) were mixed in order to make two other standards for obtaining a reliable calibration curve. The resulting calibration is shown in Figure 4-6. The error associated with weighing and mixing is reflected in the deviation of the two prepared standards from the linear response. Table 4-1 gives the certified and measured concentrations of potassium in the NIST iron ores. For determining an iron ore's concentration, the point on the calibration curve corresponding to that ore was removed from the calibration curve, and the curve was reconstructed based on the remaining points. The "unknown" iron ore concentration was then determined from the new calibration curve.

Table 4-1: Certified and measured values of potassium in NIST iron ore samples for LA-LEAFS.

NIST SRM	Certified Conc. (ppm)	Measured Conc. (ppm)
Iron Ore 690	25 ± 4	26.8 ± 0.3
Iron Ore 27f	66 ± 17	65.2 ± 0.8
Iron Ore 692	320 ± 25	313 ± 1

The selectivity of this technique was evaluated by determining if the copper ion emission line at 766.46 nm interfered with the 766.49 nm potassium fluorescence. This was

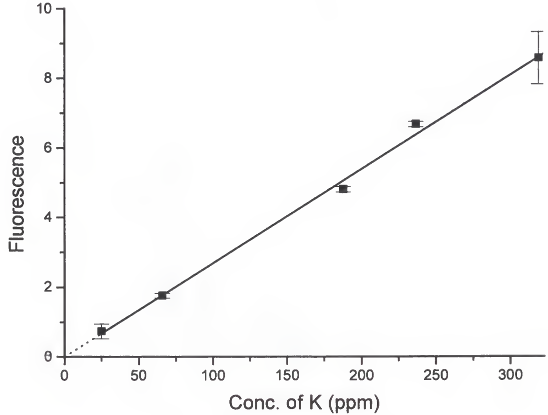

Figure 4-6: Fluorescence calibration of potassium in NIST iron ore samples.

done by comparing the LEAFS and emission spectra from a pure copper pellet and a copper pellet containing 1% potassium. These spectra are given in Figure 4-7. The emission spectra from the pure copper target shows very little emission at 766.46 nm. Only when potassium is present is there significant emission or laser excited fluorescence at this wavelength, so no interference from copper is present.

Laser source atomic absorption was also evaluated in the laser induced plasma. Rubidium was measured in NIST coal fly ash samples and potassium was again analyzed in the iron ores samples. The results are seen in Figures 4-8 and 4-9. The 3σ limits of detection for rubidium and potassium were determined to be 20 and 1 ppm respectively. The resulting absolute limits of detection were 5 pg for Rb and 0.3 pg for K. The precisions were similar to those obtained with fluorescence detection. The accuracy for LA-LAAS was determined in the same manner as that for fluorescence with the NIST iron ores. The certified and measured values for the potassium concentration are given in Table 4-2.

Table 4-2: Certified and Measured potassium concentrations of NIST iron ore samples for LA-LAAS.

NIST SRM	Certified conc. (ppm)	Measured Conc. (ppm)
Iron Ore 690	25 ± 4	21 ± 7
Iron Ore 27f	66 ± 17	58 ± 7
Iron Ore 692	320 ± 25	325 ± 14

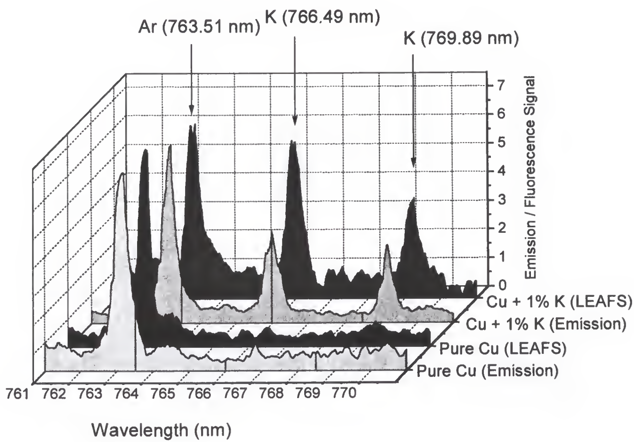

Figure 4-7: LEAFS and emission spectra of pure copper samples and copper samples which contain 1% potassium.

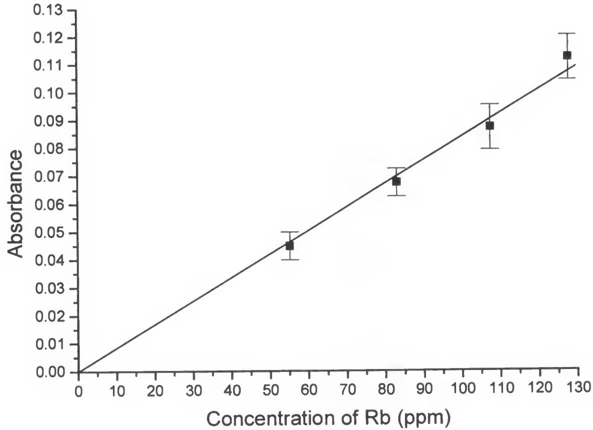

Figure 4-8: Absorbance calibration curve for rubidium in NIST coal fly ash samples.

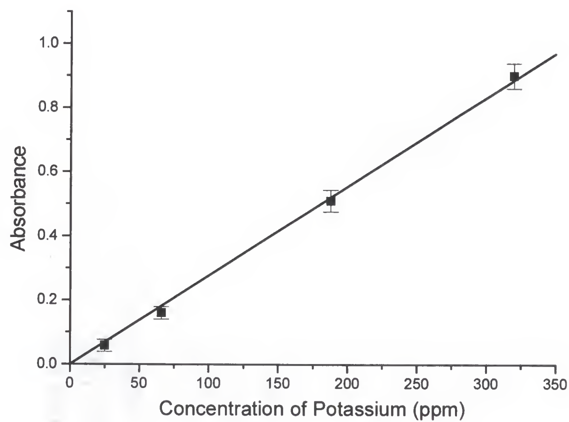

Figure 4-9: Absorbance calibration curve for potassium in NIST iron ore samples.

Temperature Measurements

The temperature in the laser induced plasma was determined by the two-line emission method. The ratio of the integral intensities of two thermal emission lines of the same element is given by

$$\frac{B_1}{B_2} = \frac{A_1 \lambda_2 g_1}{A_2 \lambda_1 g_2} \exp[(E_2 - E_1)/kT] \qquad (25)$$

where λ_1 and λ_2 are the wavelengths of the two emission lines, B_1 and B_2 are the respective emission intensities, A_1 and A_2 are the Einstein coefficients, g_1 and g_2 are the statistical weights, E_1 and E_2 are the upper energy levels, k is the Boltzman constant, and T is temperature. Since A, λ, g, and E are usually tabulated for any given transition, the temperature can be calculated from the ratio of the emission intensities [72].

The two lines used were the 465 nm and 510 nm copper emission lines, which correspond to upper energy levels of 62403 cm^{-1} and 30784 cm^{-1} respectively. A representation of how the relative intensities of the two copper emission lines change as the plasma progresses in seen in Figure 4-10. The resulting plasma temperatures at delay times of 1-20 μs are shown in Figure 4-11. The plasma temperature decays from 17,000 to 10,000 K for the first five microseconds of the plasma lifetime.

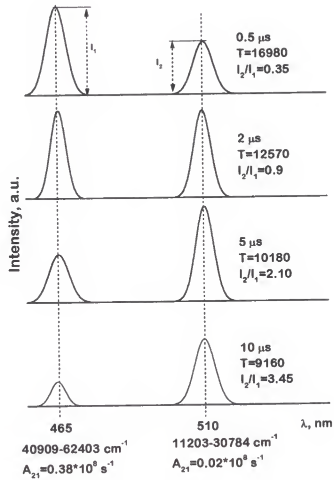

Figure 4-10: Relative change in intensities of the copper 465 nm and 510 nm emission lines for 0.5, 2, 5, and 10 microsecond delay times.

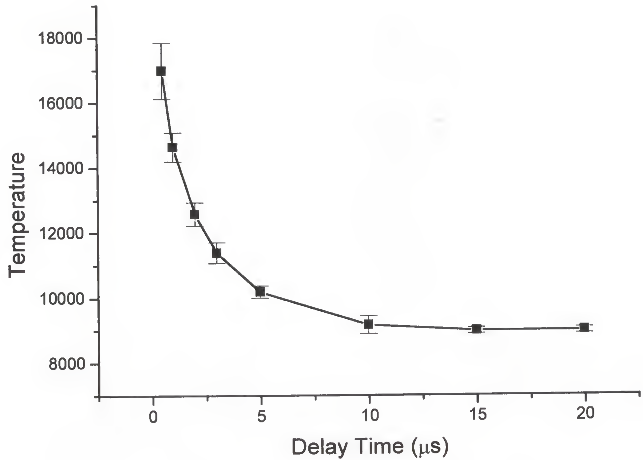

Figure 4-11: Plasma temperatures for delay times of 0 to 20 microseconds determined by the two-line emission method.

Conclusions

Laser excited atomic fluorescence and laser source atomic absorption have been used successfully to measure trace amounts of rubidium and potassium in solid samples with good precision and excellent accuracy. Both methods give a linear response with concentration. Absolute detection limits on the order of fg were obtained for LEAFS and absolute detection limits of pg were obtained for LAAS. The temperature of the laser induced plasma on a copper target was measured by the two-line emission method which indicated a high temperature of 17,000 - 10,000 K for early plasma stages of less than 5 μs.

CHAPTER 5
ISOTOPE ANALYSIS OF LITHIUM BY LASER ABLATION WITH LASER EXCITED ATOMIC FLUORESCENCE DETECTION

Introduction

Many problems in geochemical elemental analysis, and related fields, would benefit from a rapid, *in situ* technique for isotopic determinations. Traditional methods, such as thermal ionization mass spectrometry (TIMS), while generally very precise and accurate, tend to be extremely expensive and slow. Sample treatment is also laborious and time-consuming. The more recently developed technique, inductively coupled plasma mass spectrometry, is faster but normally requires the same complex sample dissolution procedures needed for TIMS.

Lithium is of particular interest because of the way in which it participates in many geological processes. Because of the relatively large mass difference between the 6 and 7 isotopes, it is a favorable candidate for isotope-selective fractionation which occurs in many geological processes and therefore it can serve as an indicator of past geological behavior. It is widely distributed throughout the Earth's crust at levels of a few ppm [75]. The average level in the earth's crust is about 20 ppm, ranging from 5 to 200 ppm in soils, 10 to 100 ppm in basalts and 60 ppm in shales [76]. Lithium isotopic determinations are also of interest in cosmological investigations, through determinations in meteorites [77], and are useful as tracers for ocean crust studies [78] and underwater hydrothermal activity [79].

By far the largest number of lithium isotopic determinations on geological samples have been carried out using TIMS. The procedure generally involves a sample dissolution and separation process. A common procedure is to grind the sample and decompose it with a low-temperature digestion in a mixture of HF and $HClO_4$. Cation exchange is often used to separate the lithium from potential interferences. The resulting solution is then placed on a rhenium filament inside the mass spectrometer and slowly heated to vaporize the sample. The most difficult problem for accurate and precise analysis is the control of the temperature-induced fractionation during the vaporization process from the filament. Common approaches include the conversion of the sample to a molecular form which exhibits minimal fractionation, such as lithium difluoride, lithium tetraborate and lithium phosphate [80]. Isotopic reference materials are also widely used to provide a correction for isotopic bias. Typically, a precision of from 0.1 to 1 % can be obtained.

Gregoire *et al.* have evaluated the use of inductively coupled plasma mass spectrometry (ICP-MS) for lithium isotope determinations [81]. Samples were digested in HF and HCl and separated using column chromatography. Isotopic reference materials were used to correct for instrumental mass discrimination. A relative precision of 0.8% was achieved for several mineralogical specimens. Although the measurement time was somewhat reduced with respect to TIMS, the complex sample dissolution and separation procedures were similarly necessary.

Isotopically selective elemental determinations can also be made using spectroscopic techniques. Lithium has a very large isotope shift, because of the relatively large difference in mass between ^6Li and ^7Li, making it a good candidate for measurement by various

spectroscopic techniques. For example, the individual isotopes have been determined by atomic absorption spectrometry by simply using mono-isotopic hollow cathode lamps as sources and a flame as the atom reservoir [82,83,84]. The idea of determining isotopes in this way was proposed as early as 1955 by Walsh [85], and was first demonstrated by Zaidel a few years later [86]. Because the isotope shift for the resonance line is about 15 pm and the lithium doublet at 670.776 nm and 670.791 nm is separated by about the same amount, the absorption line in a flame has four components with the inner peaks overlapping. The individual fine structure components have full width half maxima (FWHM) of 8-10 pm in an air-acetylene flame. Therefore, useful isotopically selective absorption measurements can be made with a moderate amount of peak deconvolution. Although the method is quite convenient and relatively inexpensive, it still involves the complicated dissolution of the sample for introduction into the flame and cannot achieve a precision better than about 0.5% because of the noise associated with the flame as an atom reservoir. Figure 5-1 shows a partial energy level diagram for the Li transition. Preliminary results will be shown below, which demonstrate the suitability of the laser ablation - laser excited atomic fluorescence technique for analyzing the lithium isotopes in a solid sample.

The laser induced plasma is nearly an ideal atom reservoir for atomic fluorescence measurements, both for plasma diagnostics and for analytical measurements. At some point in time during the life of the plasma, the entire ablated atom population must pass through a small probe volume which is efficiently excited by a dye laser beam. When the fluorescence measurement is made at a sufficient delay time with respect to the plasma formation, the background emission from the plasma is negligible. In recent studies by Gornushkin et al.,

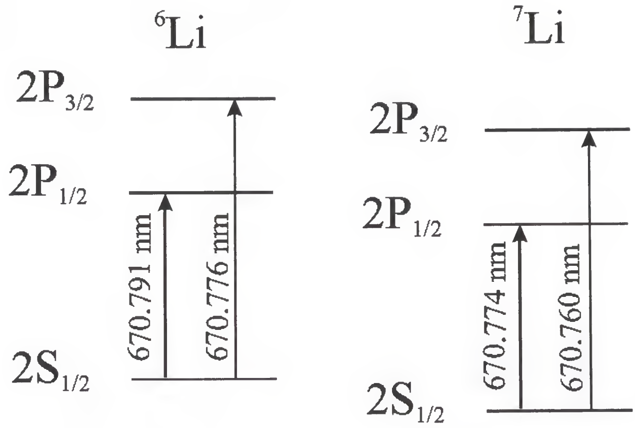

Figure 5-1: Partial lithium energy level diagram as adapted from Radzig and Smirnov [74].

laser excited atomic fluorescence (LEAFS) has been used to probe the atom population in several matrices using a UV laser (308 nm excimer) as the ablation source. One excimer laser was used as the ablation source and another was used to pump a dye laser for the fluorescence excitation. Levels of Pb in copper, brass, steel and zinc matrices were measured in the range from 0.15 ppm to 750 ppm in a low pressure atmosphere [87]. No matrix effect was observed, providing a universal calibration curve for all samples with relative standard deviations of approximately 20%. The relative and absolute limits of detection were 22 ppb and 0.5 fg, respectively. In another study with the same laser systems, cobalt was determined in soil, steel and graphite matrices [88]. In this experiment, the cobalt was excited, after a delay of 16 μs, from a level which was already populated in the ablation plasma and was monitored at the Stokes-shifted wavelength. Detection limits in the ppb to ppm range and linearity over about four orders of magnitude were obtained. Excellent correlation of the LA-LEAFS with laser ablation ICP-MS and with certified values for Co in an SRM soil standard were shown. The absolute limits of detection ranged from 30 fg to 500 fg in the three matrices.

The goal of this work was to examine the principal capability of this LA-LEAFS system to resolve the isotopic structure of lithium and to obtain some preliminary quantitative results of the isotope ratio analysis.

Experimental

The LA-LEAFS instrumentation is shown in Figure 5-2. The ablating laser (Questek 2000 Series Excimer, 308 nm), triggered by a pulse generator (Hewlett Packard 8003A) at

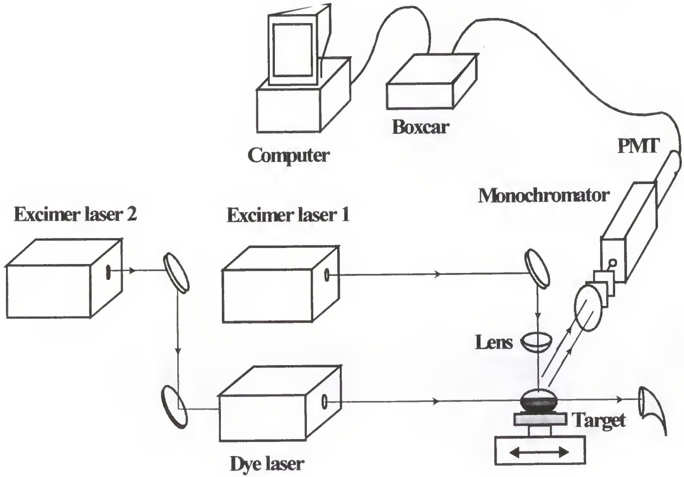

Figure 5-2: Experimental apparatus for isotope analysis by LA-LEAFS.

a frequency of 10 Hz, was directed through the quartz window into a small chamber containing a solid sample. The laser beam was weakly focused onto the surface of the sample using a biconvex quartz lens (FL = 70 mm) to produce an irradiance of approximately $5 \cdot 10^7$ W/cm^2 on the surface. The cubic chamber (5 cm x 5 cm x 5 cm), which was made of stainless steel and had quartz windows on each face, was designed to be compatible both with vacuum and a controllable gas atmosphere. It was slowly moved (0.5 mm/min) as a whole in the horizontal direction providing a partially fresh spot on the surface of the sample for each consecutive ablating pulse. Approximately 2000 laser shots were delivered over 2 mm of the sample length.

Scattered light from the ablating laser was used to trigger a delay generator built into the boxcar (model SR250) which was connected with a gate scanner (model SR200, both Stanford Research Systems Inc., USA). A gate with a fixed or scanned delay triggered a second 308 nm excimer laser (LPX100, Lambda Physics GmbH, Germany), which was used to pump the Cresyl Violet 670 dye laser (EPD-330, Lumonics Inc., Canada). The dye laser output (1.5 mm × 4 mm) was directed through the plasma plume at about 0.5 mm above the surface of the sample and scanned across the 670 nm Li doublet at a speed of 0.025 nm/min.

The resonance fluorescence was collected at a right angle to the excitation beam. Two biconvex quartz lenses (f = 60 mm, 45 mm diameter; f = 100 mm, 50 mm diameter) imaged the plasma glow into a 0.24 m focal length monochromator with an effective aperture of f/3.9 and a grating blazed at 250 nm. The monochromator entrance and exit slits were 50 μm, providing a spectral bandpass of 0.16 nm.

The detection system for further signal processing included a PMT (model R928, Hamamatsu, Japan), a 300 MHz voltage amplifier (model SR440, Stanford Research Systems, Inc.) with a gain of five, and a boxcar integrator (model SR250, Stanford Research Systems Inc.) with a gate width of 25 ns. In order to maintain a linear response range for the PMT, the fluorescence signal was attenuated by a set of colored glass filters which were calibrated at the excitation and fluorescence wavelengths. The fluorescence signal was continuously monitored by a 500 MHz bandwidth oscilloscope (TDS 620A, Tektronix, USA).

A pressed pellet of pure lithium oxalate (13.6% Li) was used throughout the experiment.

Results and Discussion

One of the most important figures of merit in isotope ratio analysis is the precision; therefore, all possible sources of noise should be reduced as much as possible. One such source is the flicker noise caused by fluctuations in the fluorescence excitation laser irradiance. This noise can be avoided by operating under saturation conditions where the fluorescence becomes independent of the laser energy and is also independent of interferences caused by variations in the quenching environment. The saturation plot for Li excited at 670.784 nm is shown in Figure 5-3. The laser energy delivered to the plasma (50 μJ) in this experiment was enough to exceed the saturation pulse energy. A set of colored glass filters was used to attenuate the dye laser beam down to the 50 μJ needed to satisfied the saturation condition, and still minimize the amount of resonance laser stray light reaching the detector.

Other parameters crucial for the isotope ratio determination were also optimized: the pressure of inert gas in the ablation chamber, the delay time between the ablating and the

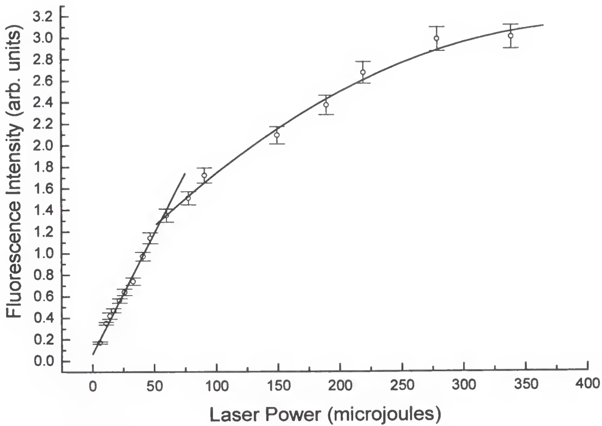

Figure 5-3: Fluorescence saturation curve of lithium.

exciting laser, the irradiance of the ablating laser, and the measurement height above the surface for the fluorescence excitation. Figures 5-4 and 5-5 show the effect of pressure and the delay time on the fluorescence intensity and on the spectral resolution. As one can see from Figure 5-4, at pressures below 100 mTorr a fine isotope structure containing three peaks of the 670.8 nm Li doublet can distinctly be resolved, but at higher pressures the structure disappears. Clearly, line broadening and, correspondingly, pressure and temperature within the plasma plume are much higher in a shielding atmosphere than in a vacuum, at least at a delay time of 1.6 μs after the plasma was ignited. Increasing the delay time at an optimum pressure of 10 mTorr (Figure 5-5) does not affect the resolution but leads to a significant decrease in the signal intensity caused by diffusion and chemical reduction of neutral Li atoms in the cooling plasma.

Figure 5-6 shows the resulting fluorescence spectrum (taken 1 cm above the sample surface) with the isotopic components labeled. The shaded area in Figure 5-6 shows the deconvoluted peaks for the two isotopes obtained using a Lorentzian line profile. As discussed above, the inner two peaks overlap completely while the outermost pair can be used for determination of the ^{7}Li / ^{6}Li ratio. The resolution is limited by the spectral bandwidth of the dye laser, which is 10 pm. An estimate of the Li isotope ratio from the data similar to that shown in Figure 5-6 and obtained in 10 consecutive scans gives a value of 12.1± 0.5 which is close to the generally accepted natural abundance ratio of 12.33 [89]. The precision can further be improved by using a higher laser repetition rate and increasing the number of scans. However, it was discovered during the course of this work that salts which are purchased from a supplier have uncertain lithium isotope abundances because the ^{6}Li has been

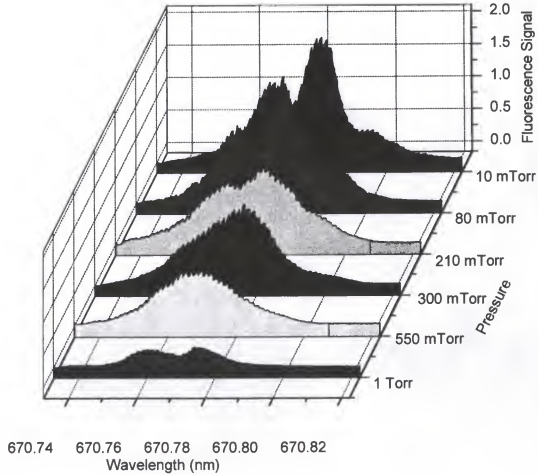

Figure 5-4: Optimization of the argon atmosphere pressure for lithium isotope determination.

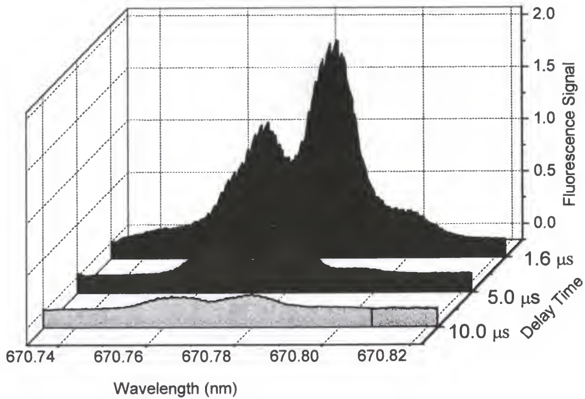

Figure 5-5: Effect of delay time on the lithium isotope fluorescence signal. These spectra were taken at an optimum pressure of 10 mT.

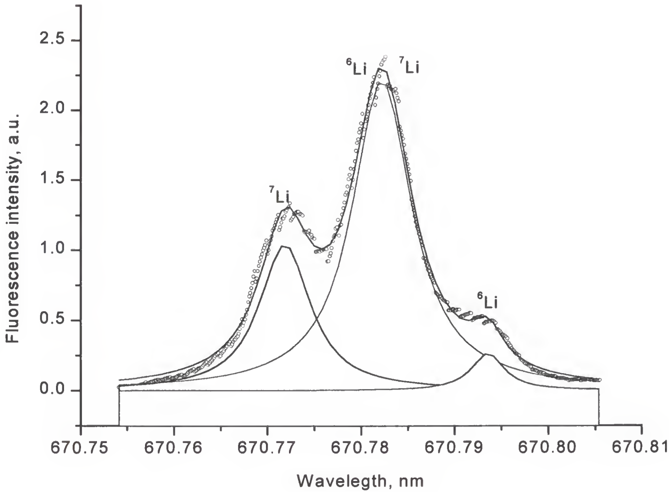

Figure 5-6: Fluorescence spectrum of lithium isotopes.

artificially depleted for sale to the U.S. Army for their thermonuclear weapons program. Therefore, an independent ICP-MS experiment was performed to confirm the isotope ratio. A 1 ppm solution of the lithium oxalate salt, which was used to make the sample pellet, was prepared. This solution was introduced into a Finnigan Quadrupole ICP-MS instrument and the lithium isotope ratio for ^{7}Li / ^{6}Li was measured and determined to be 11.95 ± 0.08.

Conclusions

The results of this study show the usefulness of high spectral resolution measurements in the laser induced plasma for the rapid and isotopically selective determination of lithium in solid samples. The error in the isotope ratio determination (currently 4 % RSD) can further be reduced by optimizing the experimental conditions. The LA-LEAFS combination possesses very good sensitivity and can provide a method for fast, direct analysis of solid samples with no sample preparation or dissolution needed.

CHAPTER 6
ISOTOPE ANALYSIS BY LASER ABLATION WITH LASER ATOMIC ABSORPTION DETECTION

Introduction

Isotope selective analysis is of important analytical interest because of the uses of isotopes in geological dating methods and monitoring of high level radioactive wastes [90-95]. Rubidium has two significant isotopes, ^{85}Rb and ^{87}Rb with a natural abundance of 72.2% and 27.8% respectively [96]. The ^{87}Rb isotope decays by emission of an electron to form stable ^{87}Sr with a half-life of 4.88×10^{10} yr. Therefore, the Rb-Sr method is used as an atomic clock which dates geological systems by constructing an isochron based on the comparison of ^{87}Rb and ^{87}Sr concentrations. The age of the system can be determined from the slope of the isochron [62]. Rubidium is also important because it is one of the products of the fission of uranium-235, and therefore it is a component of radioactive wastes. When the fission of ^{235}U occurs, it splits asymmetrically into two unstable fragments, and these fragments then undergo beta-minus decay to reach a stable nucleus. The fission yield of mass 87 is 2.55%, and the yield of mass 85 is 1.32% [97].

The field of isotope analysis has been dominated by mass spectrometric (MS) techniques which require elaborate sample dissolution and pre-treatment procedures before analysis. Laser Induced Breakdown Spectroscopy (LIBS) is gaining much popularity as a method for direct analysis of solid samples [98,99,100], and LIBS has been shown to provide

a simple, rapid technique for direct isotope analysis. Niki and coworkers [101] demonstrated the use of LIBS for measuring the isotope ratio of boron by observing the emission bands of the BO molecule produced at low pressure. A Nd:YAG laser was used to create a plasma on a boron disk inside a low pressure chamber and the emission was collected with a monochromator and a PMT. Pretsch, Petit, and Briand reported the determination of the isotope ratio of ^{238}U and ^{235}U by optical emission spectroscopy in a laser induced plasma at reduced pressure. They used a XeCl laser to produce the plasma on solid samples of natural and enriched uranium, and they reported a relative standard deviation of five percent in the isotope ratio measurements [102].

Among other spectroscopic methods for isotope analysis, Laser Source Atomic Absorption spectrometry (LAAS) is to be considered a highly selective spectrometric technique [103,104]. Wizeman and Niemax were able to resolve hyperfine components of ^{6}Li and ^{7}Li as well as ^{87}Rb and ^{85}Rb by Doppler-free absorption techniques in a graphite furnace [105]. In another paper, Wizeman and Niemax have also demonstrated isotope ratio analysis of lead by Doppler-free saturation spectroscopy in a graphite furnace. The lead isotope shifts were measured using frequency doubled diode laser radiation at 405.8 nm, and calibration using isotope dilution was demonstrated [106].

This paper reports the first use of laser ablation combined with LAAS to resolve the isotope structure of the rubidium D2 transition and to measure $^{85}Rb/^{87}Rb$ isotope ratio. A narrowband laser is focused onto the plasma plume formed on a solid calcium carbonate sample inside a low pressure chamber and scanned across the rubidium isotope structure.

This experiment provides a simple, accurate means of isotope analysis of solid samples without sample dissolution and with minimal sample pretreatment.

Experimental

The experimental arrangement is shown in Figure 6-1. A Nd:YAG laser (Quantel Brilliant, France) at 100 mJ, 7.3 Hz, and 1064 nm is focused onto the surface of a solid sample to form a plasma. The sample is mounted inside a 6 cm x 6 cm x 6 cm stainless steel chamber with a controlled atmosphere of argon which was maintained by a precision needle valve and monitored with a pressure gauge (model # 221AHS, Baratron, USA). The plasma was probed by the 780.02 nm radiation of a Ti:Sapphire laser (Schwartz-Electro Optics, Titan series, USA) which was pumped with a 5.0W Argon Ion laser (model# 2060, Spectra Physics, USA). The Ti:Sapphire laser was operated in the ring mode with a spectral bandwidth of 400 MHz. The ability to scan the laser was provided by an in-house construction including an intercavity Fabery-Perot etalon mounted onto a precise rotation stage. The rotation stage was connected to a stepping motor (model# EPC-015, Hurst, USA) of variable speed via two wheel-and-belt reduction stages which were used to provide smooth tuning. This construction allowed the Ti:Sapphire 400 MHz line to be scanned over the bandwidth of the birefringent filter profile of the laser, which was approximately 2 GHz.

The Ti:Sapphire beam was split with a 95/5 beam splitter and chopped at 7.3 Hz with an acousto-optic modulator (Model DLM-40V-7, Anderson Laboratories, Inc., USA). The first portion of the beam was aligned onto the plasma, and the second portion of the beam was aligned onto the cathode inside a rubidium hollow cathode lamp (Fisher Scientific, USA)

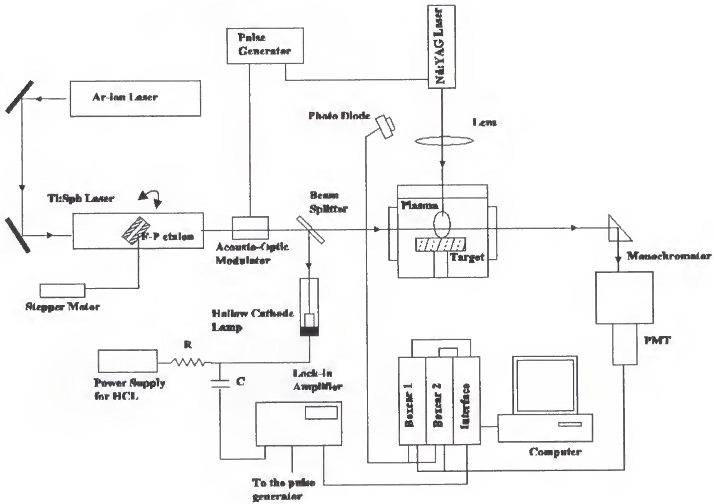

Figure 6-1: Experimental arrangement for LA-LAAS isotope analysis.

in order to induce the opto-galvanic effect. The opto-galvanic effect occurs when a discharge is irradiated with a strong laser field resonant with an atomic transition of a species which is present in the discharge. This effect is measured by observing the change in the steady-state current of the discharge when the laser field is present [72]. The opto-galvanic signal was collected from the hollow cathode lamp with a lock-in amplifier (model 128A, EG&G Princeton Applied Research, USA) using the acousto-optic modulation frequency as the reference frequency for the lock-in amplifier. The opto-galvanic signal provided a well characterized reference spectrum of the rubidium isotopes for all absorption spectra. This was necessary in order to determine the exact wavelength scale of the LA-LAAS spectra because the in-house constructed Ti:Sapphire scanning system was not calibrated. The opto-galvanic signal was collected simultaneously with each atomic absorption signal and the correct wavelength scales assigned. The opto-galvanic signal collection arrangement is also shown in Figure 6-1.

The Ti:Sapphire laser radiation probing the plasma was attenuated with neutral density filters such that the probe beam was reduced to 0.8 mW, giving a spectral irradiance of 0.64 W cm^{-2} nm^{-1} which was below the atomic absorption saturation irradiance level. Two pin-hole filters were placed between the sample chamber and the PMT in order to spatially reduce the amount of plasma emission reaching the detector. The PMT (R636, Hamamatsu, Japan) was mounted onto a monochromator (Digikrom 240, CVI,. USA) which was used to spectrally filter the intense plasma emission. A pulse generator (model 802, Wavetek, USA) was used to trigger the Nd:YAG laser and the acousto-optic modulator at a frequency of 7.3 Hz. The TTL pulse of the pulse generator was used as the reference signal into the lock-in

amplifier for the opto-galvanic signal detection scheme, and the scattered emission from the Nd:YAG laser was detected by a photodiode and used to trigger the boxcars and the computer interface.

The transmittance spectrum was collected by scanning the Ti:Sapphire across the rubidium transition. During each scan, 1000 ablation shots were delivered to the target, and each spectrum was an average of five scans. Two identical boxcars (model SR250, Stanford Research Systems, USA) were used to process the transmitted and reference signals received from the PMT. Figure 6-2 shows the timing diagram of the signal collection. The first boxcar was used as the signal channel and was set to a gate width of 500 ns and to a delay time between 1.4 - 300 μs, within which a fraction of laser radiation was absorbed (I). The second channel was set to a delay of 3 ms and a gate width of 500 ns. At this delay time, no absorption of resonance laser light occurred due to complete decay of the plasma providing the 100% transmission signal (I_0). The fraction of light transmitted through the plasma (I/I_0) was measured and converted to absorbance.

The series of $CaCO_3$ samples was prepared by using a high purity CaO powder (Aldrich Chemicals, USA) mixed with aqueous standard solutions of RbCl (Fisher Scientific, USA) in open air. After the solution was added to CaO, a vigorous exothermic reaction occurred by capturing CO_2 from the air and releasing H_2. The paste-like sample was then carefully stirred, dried over night in an oven, and pressed into pellets.

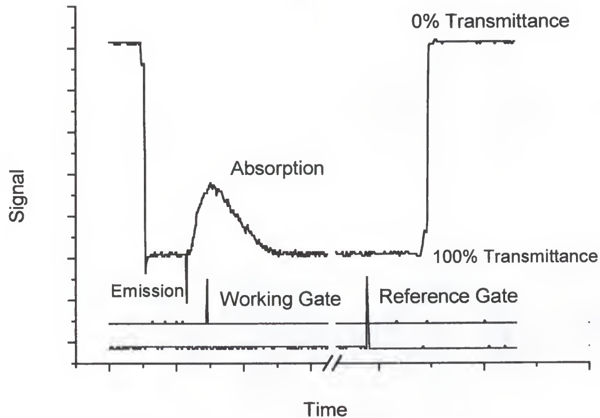

Figure 6-2: Experimental timing diagram for collection of the LA-LAAS signal. The working gate was set to 1.4 - 300 μs, and the reference gate was set to 3 ms. The gate widths were 500 ns.

Results and Discussion

Optimization of the isotope measurements of rubidium

A partial energy level diagram of rubidium illustrating the D2 transition is shown in Figure 6-3. The isotope structure arises from the splitting of the $5S_{1/2}$ level, but the hyperfine structure resulting from the splitting of the $5P_{3/2}$ level could not be resolved. The atomic absorption signals of the two rubidium isotopes were optimized for probe laser spectral irradiance, measurement height, delay time, and resolution. The available Ti:Sapphire probe intensity was attenuated 0.64 W $cm^{-2}nm^{-1}$ in order to avoid saturation of the atomic absorption transition, which occurs when the rate of atomic absorption is equal to the rate of stimulated emission, so no net absorption is observed. The saturation curve shown in Figure 6-4 was obtained using a $CaCO_3$ sample with a rubidium concentration of 500 ppm. It is seen in Figure 6-4 that as the spectral irradiance increases, the atomic absorption decreases.

The height of the probe beam and measurement delay time were also optimized simultaneously as they were strongly dependent on one another. Indeed, as the probe region was chosen farther from the surface, the density of absorbing species reached its maximum as the delay time increased due to a finite speed of plasma propagation. However, at large distances from the surface the number of absorbers is negligible due to the decrease of their number density as $1/r^3$, where r is the distance from the sample surface. A probe height of 1.0 mm above the sample surface was found to be optimal providing a strong signal and the best spectral resolution at any delay time. These conditions correspond to the rear of the expansion zone at a time when the electron density is lowest. We also studied how the resolution of the isotope peaks depended upon pressure at different delay times. A plot

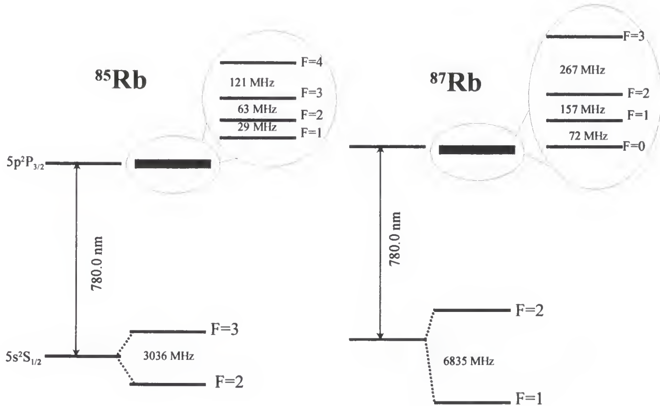

Figure 6-3: Partial energy level diagram illustrating the D2 transitions in ^{85}Rb and ^{87}Rb as adapted from Radzig and Smirnov [74].

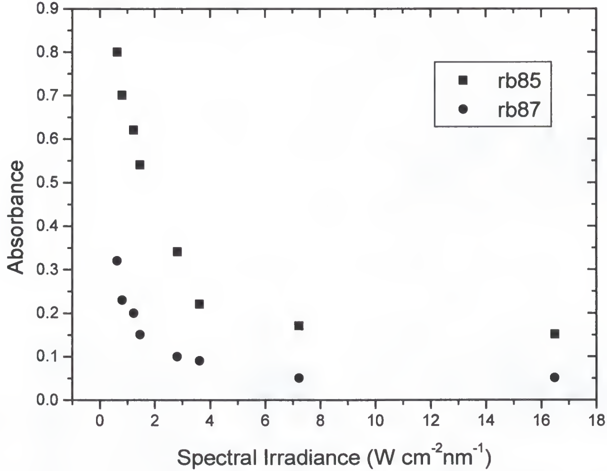

Figure 6-4: Absorption saturation plot for rubidium.

showing rubidium line profiles as a function of pressure and delay time is shown in Figure 6-5. These spectra were obtained using a $CaCO_3$ sample containing 500 ppm Rb. The top spectrum in each column is a rubidium hollow cathode lamp spectrum shown for comparison. It can be seen that at a delay time of 1.4 μs the isotope structure is unresolved, and the entire rubidium linewidth is approximately 30 pm. As the delay time increases from 5 μs to 20 μs, the isotope structure is clearly seen, and the line widths do not show significant dependence on ambient pressure up to 10 Torr. In the laser induced plasma at longer delays, the line widths (FWHM) are 2.5 - 3.0 pm which compare well to the hollow cathode lamp widths of 2.3 pm, FWHM. A resolved rubidium isotope spectrum for a low pressure of 150 mTorr, a long delay time of 120 μs, and a calcium carbonate sample of 1000 ppm Rb is shown in Figure 6-6. Therefore, one can see that the conditions can be optimized for spectral resolution or for increased sensitivity by choosing the appropriate pressure and delay time. In these experiments, a pressure of 150 mTorr, a delay time of 100 μs or greater, and relatively large concentrations of Rb were chosen for obtaining resolved spectra. Pressures of 1-10 Torr and delay times of 5-20 μs were chosen in order to obtain larger absorption signals for smaller Rb concentrations at the expense of resolution.

Line Broadening in the Laser Induced Plasma

The observed line widths in this experiment were compared to the theoretical estimated line widths for rubidium in a low pressure plasma in order to understand the line broadening mechanisms which prevailed in the plasma and to obtain fundamental plasma parameters such as electron number density and temperature at pressures below 10 Torr.

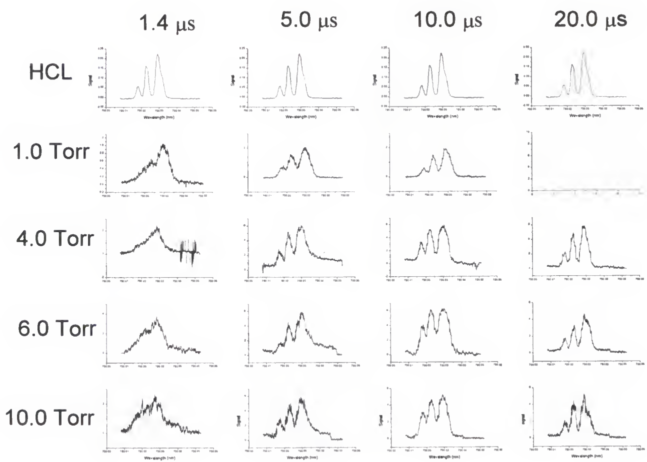

Figure 6-5: Rubidium absorbance spectra illustrating the dependence upon pressure and delay time. There was no signal for 20 μs and 1.0 Torr at the rubidium concentration used for this graph.

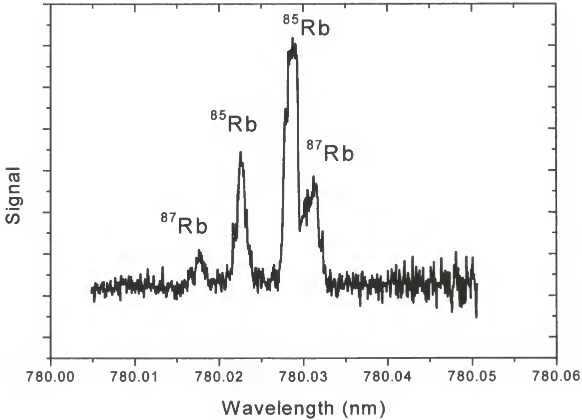

Figure 6-6: Resolved rubidium isotope spectrum. This spectrum was obtained at a pressure of 150 mTorr and a delay time of 120 μs.

There are four possible line broadening mechanisms in a laser plasma coupled with LAAS detection: Doppler broadening, collisional broadening (Lorentzian), Stark broadening, and probe laser field broadening (saturation broadening). Figure 6-7 represents the theoretical estimation of rubidium line widths as a function of temperature for Doppler, collisional, and Stark broadening.

Doppler broadening is the most likely broadening mechanism in a low pressure laser plasma at a lifetime of several microseconds under optically thin conditions. Optically thin conditions are met with trace analyte concentrations or with the use of weak transitions. Doppler broadening results from the statistical distribution of velocities of the absorbing atoms along the observation path. In thermal equilibrium, the distribution of velocities is given by Maxwell's Law and the Doppler broadened with is [107]

$$\Delta\lambda_D(T) = \lambda_0\sqrt{\frac{8kT\ln 2}{mc^2}} \qquad (26)$$

where λ_0 is the wavelength in the center of the absorption line, k is the Boltzmann constant, T is the absolute temperature, m is the atomic mass, and c is the speed of light. According to the theoretical curve for a Rb line width of 3 pm, as was measured in this experiment, the kinetic or translational temperature can be estimated to be 3000 K.

Broadening of atomic transitions can be caused by collisions with surrounding particles. The amount of broadening caused by collisions increases with the concentration of perturbers, so collisional broadening is also refered to as pressure broadening. Theoretical collisional broadening is represented by three lines in Figure 6-7 taken for three different

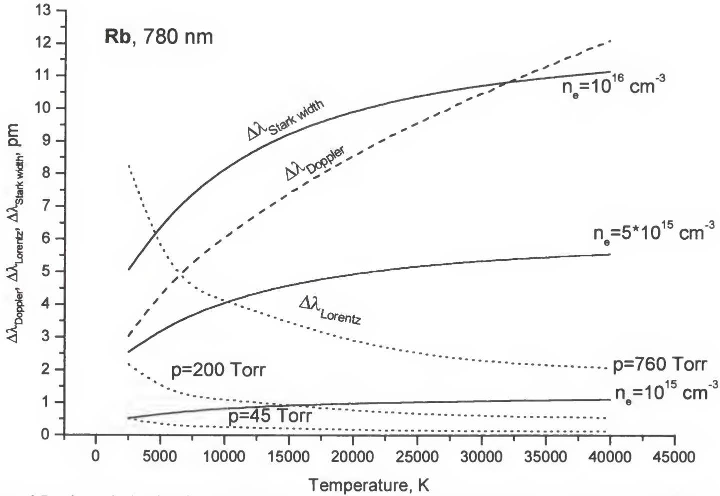

Figure 6-7: Theoretical estimation of rubidium line widths in a laser induced plasma as a function of temperature and attributed to Doppler broadening (----), collisional broadening (••••) for three pressures, and Stark broadening (—) for three electron number densities.

pressures: 45 Torr, 200 Torr, and 760 Torr. The following equation was used to evaluate the collisional broadening [107]

$$\Delta\lambda(T) = \frac{2\lambda_0^{\,2}}{\pi ckT} p[2\pi RT(\frac{1}{M_1} + \frac{1}{M_2})]^{1/2}\sigma \qquad (27)$$

where λ_0 is the transition wavelength, c is the speed of light, T is the absolute temperature, p is the argon pressure, R is the universal gas constant, σ is the collisional cross section and M_1 and M_2 are the atomic weights of the colliding species, Rb and Ar atoms in this case. The value taken for σ was 100 Å^2, as suggested by Parsons, Smith, and Bentley as a reasonable estimation of this parameter [108]. As can be seen in the theoretical plot, the collisional broadening does not contribute much to the line width until the pressure approaches atmospheric pressure. In the experiment, the working pressures were less than 10 Torr; therefore, this type of broadening could be neglected.

Stark broadening is considered to be a main source of broadening in atmospheric pressure plasmas because of the high electron number densities found in these plasmas [109]. Stark broadening occurs when an emitting atom at a distance r from an ion or electron is perturbed by the electric field associated with that ion or electron. The expected Stark broadening and Stark shift can be calculated from two simplified equations for electron-impact and ion-broadening approximations [107].

$$\Delta\lambda_{\frac{1}{2}} = [1 + 1.75x10^{-4} n_e^{\frac{1}{4}} \alpha(1 - 0.068 n_e^{\frac{1}{6}} T^{-\frac{1}{2}})] w n_e \qquad (28)$$

$$\Delta\lambda_{shift} = [\frac{d}{w} + 2x10^{-4} n_e^{1/4} \alpha (1 - 0.068 n_e^{1/6} T^{-1/2})] 10^{-16} w n_e \qquad (29)$$

Equation 28 was used to calculate the line width, and equation 29 was used to calculate the line shift. In these expressions n_e is the electron number density, w is the electron impact half width, d/w is the relative electron-impact shift, and α is the ion broadening parameter. The parameters w, d/w, and α were not available for the Rb D2 transition, but could be estimated from the known set of parameters for the two adjacent alkaline elements, potassium and cesium [106]. It was found by Zhao, et. al. that electron number densities for delay times between 1 and 10 μs fell between 10^{17} cm^{-3} and 10^{16} cm^{-3} for aluminum and magnesium samples at 100 Torr argon pressure [109]. These values are at least one order of magnitude higher than the values that were deduced from our experiment which were estimated using the experimental linewidths of 2.5-3.0 pm and equation 28. This can be seen in Figure 6- 7 where the solid line represents the rubidium Stark broadened line widths as a function of temperature and electron number density. The temperature used in the Stark broadening equations is the excitation temperature, and this temperature was estimated for this experiment by the two emission line method [72]. The two lines used were the 585 nm and 616 nm calcium emission lines. The excitation temperature was found to be 12,000 ± 1000 K at a delay time of 4 μs. Comparing the observed experimental line widths with those expected from Stark broadening for this excitation temperature, it can be seen that the Stark effect is not dominant with respect to Doppler broadening and the electron number density has an upper limit of $5x10^{15}$ cm^{-3}. It can also be seen from Figure 6-5 that there is no Stark

shift present in the rubidium spectra. This also indicates that the quadratic Stark effect is less significant than Doppler broadening.

The last mechanism, laser field broadening, can occur when the spectral irradiance of the probe laser is above the absorption saturation threshold [110]. Since the saturation level of the rubidium transition was determined during optimization and the probe laser irradiance was well below the saturation value, this type of broadening could be neglected. On the basis of the data presented, it can be concluded that Doppler broadening is the main contribution to the observed line widths. Furthermore, the different electronic and translational temperatures indicated the absence of thermodynamic equilibrium.

Isotope Ratio Determination

The analytical data reported in this section were all collected at optimal conditions for sensitivity. These conditions were a pressure of 2.5 Torr, a measurement height of 1.0 mm above the sample surface, a probe power of 0.8 mW, and a delay time of 75 μs. The ^{85}Rb / ^{87}Rb ratio was determined for solid $CaCO_3$ pellets with varying rubidium concentrations (200-1100 ppm) by taking the ratio of the peak absorbance values for ^{85}Rb and ^{87}Rb for each of twenty spectra and then averaging them. This ratio was determined to be 2.7 ± 0.2, which was confirmed by an independent ICP-MS experiment to be 2.68 ± 0.03. For the ICP-MS analysis, a one ppm rubidium aqueous solution was prepared from the same stock RbCl solution used to prepare the $CaCO_3$ samples. This one ppm solution was introduced into an ICP-MS (Finnigan quadrupole, USA), and the isotope ratio determined by comparing the peak intensities of the two isotopes.

The rubidium isotope ratio is also reflected in the slopes of the LA-LAAS isotope selective calibration curves. The calibration plots are given in Figure 6-8, and the ratio of the

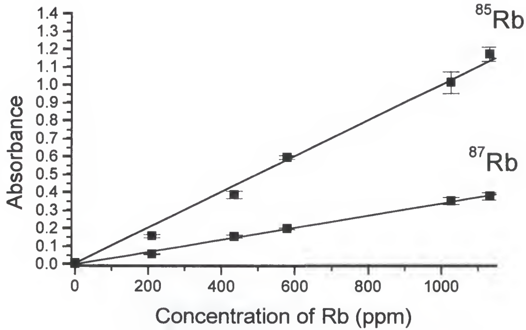

Figure 6-8: Isotope selective calibration plot of rubidium. The slope of the ^{85}Rb curve is 9.9×10^{-4} Abs. Units/ppm, and the slope of the ^{87}Rb curve is 3.6×10^{-4} Abs. Units/ppm. The ratio of the slopes is 2.75.

^{85}Rb slope to the ^{87}Rb slope is 2.75. Both calibration curves were obtained with a precision of 5% RSD and a 3σ LOD equal to 24 ppm for both ^{85}Rb and ^{87}Rb.

The mass ablated per laser shot was estimated by weighing a fresh $CaCO_3$ sample pellet, making 30,000 laser shots on the surface of the sample, and again weighing the sample in order to determine the total mass ablated. The total mass ablated was divided by the total number of laser shots to obtain the value for the mass ablated per laser shot. Taking into account this value, the absolute LOD can be calculated. This value is 20 pg for each isotope. This compares well to the Doppler-free LAAS in a graphite furnace LOD of 1.4 pg and 1.3 pg for ^{85}Rb and ^{87}Rb respectively reported by Niemax and coworkers for the rubidium isotopes [105].

Analytical Applications

This method was used to determine the isotope ratio and isotope concentrations of rubidium in a real geological sample. A powdered basalt rock was obtained from the University of Florida Department of Geology for analysis. The powdered rock was divided into equal portions and varying concentrations of the RbCl solution were added to each portion to provide samples for a standard additions experiment. The samples were mixed well, dried for twenty-four hours, and pressed into pellets. The pellets were analyzed by the LA-LAAS procedure described in this paper, and a typical standard additions plot obtained (Figure 6-9). The measurement precision was again 5% RSD, and the total rubidium concentration in the basalt was determined to be 77 ± 5 ppm rubidium. The isotope ratio of

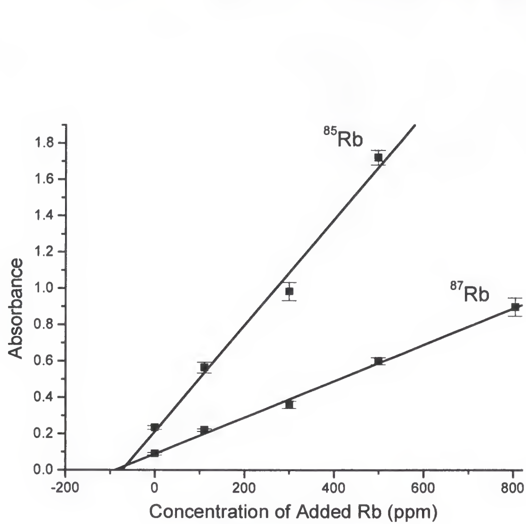

Figure 6-9: Isotope selective standard additions plot of rubidium in basalt rock.

^{85}Rb / ^{87}Rb in the basalt rock was determined to be 2.8 ± 0.3 by comparing the peak absorbance values of the individual isotope peaks in spectra taken of the basalt rock. Taking into account the isotope ratio of rubidium in the basalt, the actual isotope concentrations could be determined. These were 55.6 ppm and 21.4 ppm for ^{85}Rb and ^{87}Rb respectively. These results show that the LA-LAAS technique is applicable for determining rubidium isotope concentrations and isotope ratios in geological samples.

Conclusions

It has been shown that isotopes such as ^{85}Rb and ^{87}Rb which are characterized by small isotopic shifts can be resolved in a laser induced plasma under optimized conditions. With an argon atmosphere of less than 10 Torr, and working at a delay time of 100 μs, the D2 transition lines of ^{85}Rb and ^{87}Rb have been successfully resolved and measured. The isotope ratio was determined in solid calcium carbonate samples to be 2.7 ± 0.2 with a RSD of 5% and with a limit of detection of 25 ppm or 20 pg per laser shot for each isotope. The analysis of a basalt rock sample was also done. The isotope ratio was found to be 2.8 ± 0.3, and the total rubidium concentration was determined to be 77 ppm with a precision of 6 percent RSD.

In general, this technique provides a rapid, non-invasive method for isotope ratio determinations in solid samples. The precision of the isotope ratio measurements could be greatly improved by probing a single plasma simultaneously with two diode lasers tuned to the ^{85}Rb and ^{87}Rb transitions respectively instead of measuring each isotope individually in sequential plasmas as was done in this case.

CHAPTER 7
CURVE OF GROWTH TECHNIQUE APPLIED TO LASER INDUCED PLASMAS

Introduction

The character of the analytical calibration function for emission spectroscopy in laser induced plasmas generally involves the entire range of spectrochemical conditions from optically thin to optically thick behavior. For strong resonance lines, non-linearity is often observed for concentrations in solid samples of the order 0.1 - 1 %. The application of the well-known model for emission spectroscopy, using the concept of the curve-of-growth (COG), is considerably complicated for these plasmas. The plasma is composed primarily of only slightly diluted atoms, ions and particles of the sample, and therefore its spectrochemical behavior (temperature, electron density, line broadening) is heavily influenced by the total composition of the matrix. Moreover, the plasma evolves rapidly in time and space and never quite develops a homogeneous temperature. Practical spectrochemical measurements are usually made several microseconds after the initiation of the plasma breakdown, when recombination processes have produced a suitable plasma environment. At this stage in the plasma lifetime, an estimate of an electronic excitation temperature is possible from a Boltzmann plot, even though local thermodynamical equilibrium (LTE) may not exist. Despite the theoretical and experimental complexities, it appears that an examination of the fundamental nature of the analytical calibration function in laser-induced

plasmas, in terms of the concept of the COG, might prove useful in improving the performance of these plasmas for spectrochemical analysis. Such observations should prove useful in ascertaining the possible linear dynamic range for a given measurement and assist in the selection of the most appropriate spectral transitions for quantitative analysis.

The concept of the COG in emission spectroscopy was first experimentally investigated by Ladenburg and Reiche in the early 1900's [111] and then developed in detail by Mitchell and Zemansky [112], van der Held [113], and a few other researchers in the 1930's. Experimentally, these pioneering works were based on the use of resonance vapor lamps both as a light source and as an absorbing cell. Later in the 1950's, Hinnov [114] and Alkemade and Hollander [115, 116] developed the COG method for flame spectroscopy. Special investigations of the COG have been reported in numerous publications; some examples include the study of the general shapes of COG in atomic absorption, emission and fluorescence [117-119], the effect of line profile characteristics on COG measured in flames [120], the analytic approximations for COG calculations [121-122], and astrophysical application of the COG for the determination of stellar temperatures and elemental abundances [123].

The goal of this work was to apply the COG concept to the laser-induced plasma in order to obtain useful information about the analytical plasma characteristics, such as limits of calibration linearity and spectral line behavior, as well as to estimate several fundamental plasma parameters such as atom number densities and optical crossections.

Theoretical

The curve of growth (COG) is a function $I=f(n_0)$, where I is the integrated emission intensity and n_0 is the number density of ground state atoms which related to the analyte concentration in the sample. According to the classical theory [124], the spectral line intensity is determined by the equation

$$I = \alpha \frac{8\pi hc}{\lambda^3} \frac{n_1}{n_0} \frac{g_1}{g_0} \int (1 - e^{-k(\nu)l}) d\nu \qquad (30)$$

where α is the constant factor depending on the measurement instrumentation, h is Planck's constant (J s), c is the speed of light (m s^{-1}), λ is the transition wavelength (m), n_1, n_0, g_1, and g_0 are the number densities (cm^{-3}) and the degeneracies (dimensionless) of the upper and the ground atomic levels (for the resonance transition), correspondingly, $k(\nu)$ is the frequency dependent absorption coefficient (cm^{-1}), and l is the absorption length (cm).

The frequency dependence of the absorption coefficient $k(\nu)$ is given by [112,124,125]

$$k(\nu) = k_0 \frac{a}{\pi} \int_{-\infty}^{\infty} \frac{e^{-t^2} dt}{(t - x)^2 + a^2} \qquad (31)$$

where k_0, a, and x are defined as follows:

$$k_0 = 2\pi^{3/2} \frac{e^2}{m_e c} \frac{n_0 f}{b}, b = \frac{\pi \Delta \nu_D}{\sqrt{\ln 2}} \qquad (32),$$

$$a = \frac{(\Delta \nu_N + \Delta \nu_L)}{\Delta \nu_D}\sqrt{\ln 2} \approx \frac{\Delta \nu_L}{\Delta \nu_D}\sqrt{\ln 2} \qquad (33),$$

$$x = \frac{2(\nu - \nu_0)}{\Delta \nu_D}\sqrt{\ln 2} \qquad (34).$$

In the above equations, e is the elementary charge (C), m_e is the electron mass (kg), f is the transition oscillator strength (dimensionless), ν_0 is the frequency of the center of the line (Hz), $\Delta\nu_N$, $\Delta\nu_L$, and $\Delta\nu_D$ are the natural, Lorentzian, and Doppler line half-widths (Hz), correspondingly. The two latter quantities can be expressed by [124]

$$\Delta \nu_L = \frac{2p}{\pi k T}[2\pi RT(\frac{1}{m} + \frac{1}{M})]^{1/2}\sigma \qquad (35) \text{ and}$$

$$\Delta \nu_D = \frac{\nu_0}{c}(\frac{8\pi kT}{m})^{1/2}\sqrt{\ln 2} \qquad (36)$$

where p is the pressure of perturbing species (Pa), R is the universal gas constant (J mol^{-1} K^{-1}), T is the absolute temperature (K), m and M are the masses (kg) of the emitting atom and the perturber, and σ is the collision cross section (m^2).

The spectral line intensity introduced in Equation 30 can also be rewritten in terms of total absorption A_t multiplied by a proportionality coefficient. The total absorption A_t is defined as [112,115,125]

$$A_t = 2\pi \frac{\Delta \nu_D}{\sqrt{\ln 2}} \int_0^{\infty} [1 - \exp(-\int_0^{l} k(x)dl)]dx \qquad (37)$$

where $\int_0^{l} k(x)dl$ can be replaced by $k(x)l$ for a homogeneous flame or plasma.

Finally, the double-logarithmic plot of $A_t / 2b$ vs $n_0 fl / b$ represents the theoretical curve of growth which has two asymptotes

$$\log[\frac{A_t}{2b}] = \log[\frac{\pi^2 e^2}{m_e c}\frac{n_0 fl}{b}], \text{ when } \frac{n_0 fl}{b} \rightarrow 0 \qquad (38),$$

and

$$\log[\frac{A_t}{2b}] = \log[\frac{2\pi^2 e^2}{m_e c} a \frac{n_0 fl}{b}]^{1/2}, \text{ when } \frac{n_0 fl}{b} \rightarrow \infty \qquad (39)$$

with slopes 1 and ½, respectively. Obviously, the asymptotes for the emission COG have the same form as Equations (38) and (39) but both include a constant proportionality factor. The experimental COG is usually constructed by measuring the integrated line intensity in arbitrary units as a function of the analyte concentration.

Once the curve of growth is constructed, valuable information on fundamental plasma parameters can be determined such as those listed below.

1. The *a*-parameter can be measured by comparing the experimental curve with a set of theoretical COGs. This yields information about collisional vs Doppler line broadening.

2. If the *a*-parameter is known and values *for* $\Delta \nu_L$ or $\Delta \nu_D$ are found, the plasma temperature or collisional cross section can be obtained via Equation 35 or Equation 36.

3. The $n_0 fl$ value can be determined upon matching the experimental and theoretical COGs. If the oscillator strength and the absorption length are known, the number density of ground state atoms n_0 can be found. Inversely, if n_0 and l are known, then the oscillator strength of the transition can be determined.

4. The intersection of the initial and final asymptotes marks the point where the transition from low to high plasma optical density occurs. The abscissa of this point yields the upper limit of the linear calibration range.

Experimental

A typical LIP-OES experimental arrangement consisting of a Nd:YAG laser (Quantel Brilliant, France) and a gated ICCD detector (Princeton Instruments, USA) was used. A schematic of this arrangement is shown in Figure 7-1. The laser was operated at 10 Hz and was focused onto the sample surface and aligned through a pierced mirror tilted at a 45^0 angle with respect to the laser beam. Emission light was collected from the top of the plasma using the same mirror and a simple optical system including a short focal length lens and a 0.5 m

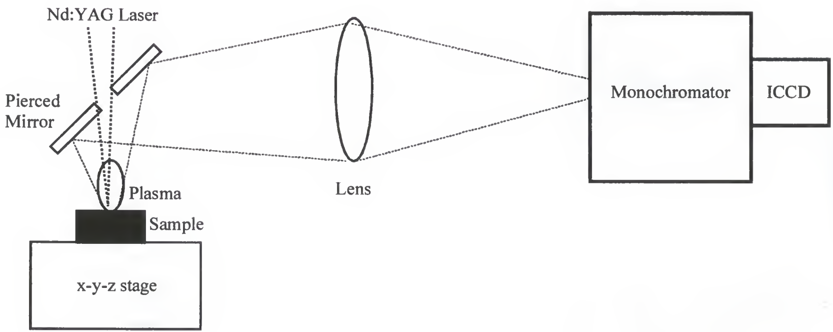

Figure 7-1: Experimental arrangement for LIP-OES.

monochromator (SpectraPro-500i, Acton Reasearch Corporation, USA) with a 2400 mm^{-1} diffraction grating.

Spectral line profiles were measured by LAAS detection using a scanning Ti:Sapphire laser (Schwartz-Electro Optics, Titan series, USA) pumped by a 5.0 W Argon ion laser (Spectra Physics, USA). The Ti:Sapphire laser beam was chopped by an acousto-optic modulator (DLM-40V-7, Anderson Laboratories, Inc., USA) at 10 Hz, frequency doubled by a non-linear crystal (lithium iodide, Quantum Technology, Inc., USA), and split into two beams by a beam splitter. One beam was aligned onto a chromium hollow cathode lamp where it induced the opto-galvanic effect, which was used for wavelength correction, and the second beam was directed through the laser plasma at a distance of 1 mm from the target surface. The Ti:Sapphire laser was scanned across the chosen atomic transition by rotating the intra cavity etalon. The opto-galvanic signal was measured with a lock-in amplifier (128A, EG&G Princeton Applied Research, USA), whereas the resulting transmission signal was collected by a PMT (R636, Hamamatsu, Japan) which was mounted onto a monochromator (Digikrom 240, CVI, USA). The monochromator was used to spectrally filter the intense plasma emission. Both signals were further processed with two identical boxcars (SR250, Stanford Research Systems, USA) set on the same gates and delay times and terminated by a PC.

Stainless steel NIST standards (1262-1265 series and 805-818 series) were used throughout the experiment. Chromium was chosen as the analyte because it was present in the steels in a large concentration range: (0.007 % to 1.3 %). Emission from the 425 nm Cr resonance line was measured for 5-10 runs performed on each sample. Each run consisted

of 20 accumulations from 20 ablation laser shots which were summed together to make a single measurement. The analytical signal was the integral emission averaged over all measurements.

Results and Discussion

The calibration plots for Cr in steel samples were measured using delay times of 0.5 μs, 2 μs, and 5 μs and gate widths of 0.5 μs and 1 μs and are shown in Figure 7-2. It can be seen from Figure 7-2 that as the delay time increases, the inflection points in the log-log plot (right column) correspond to decreasing concentrations. The inflection in the log-log calibration plot indicates where the transition between optically thin and optically thick (self-absorption) plasma conditions occur, which corresponds to a concentration of Cr in steel of about 0.1 %. At the delay time of 5 μs, the slopes of two portions of the log-log plot are almost exactly 1 and ½ in full agreement with the theoretical prediction indicating the plasma has reached thermodynamical equilibrium. Therefore, in the foregoing discussion relating a COG theory to our experiment, we will use only the data obtained for this particular delay time (5 μs). The gate width of 0.5 μs - 1 μs was chosen because the plasma temperature does not change substantially within this time interval.

Figure 7-3 shows a series of log-log calibration plots obtained for different energies of the ablation laser. Plots 1,2, and 3 were constructed using the Cr I 425 nm resonance line and plot 4 was constructed using the Cr II 206 nm resonance line. As seen from Figure 7-3 (plots 1-3), the higher the laser energy, the higher the concentration at which the plot changes slope from 1 to 0.5. This is likely due to the higher plasma temperature created by

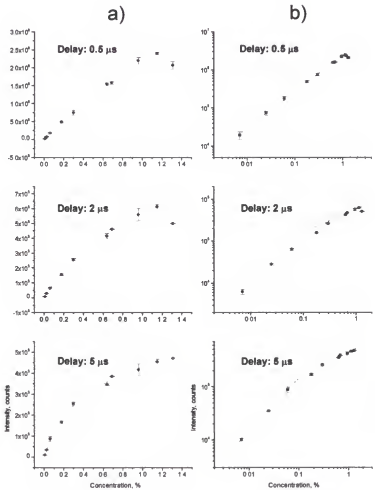

Figure 7-2: Curves of growth for Cr in stainless steel NIST standards obtained at delay times of 0.5, 2, and 5 µs with the detector gate of 1 µs. a) COGs with a linear scale, b) COGs with a log-log scale.

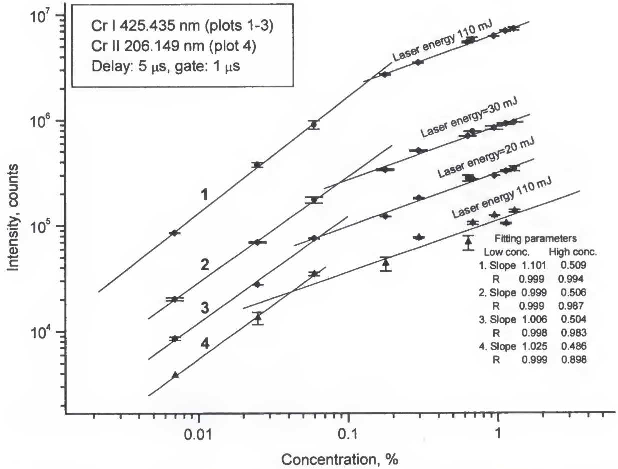

Figure 7-3: Curves of growth for Cr I and Cr II in stainless steel corresponding to different energies of the ablating laser. Intensity values are arbitrary; some of the graphs were shifted along the y-axis for better separation and representation. The critical features are the slopes and intersection points of the asymptotes.

the more energetic laser pulse. Indeed, the temperatures determined from slopes of two Boltzmann plots corresponding to laser ablation energies of 110 mJ and 20 mJ (Figure 7-4) yielded the values of 8700 K and 7900 K, correspondingly. The Boltzmann plots were constructed using iron emission lines between 423 nm and 431 nm. We can therefore conclude that the higher the temperature, the higher the degree of excitation and ionization, and the smaller the number of ground state neutral atoms responsible for self-absorption.

Thus, once we have experimental COGs (Figure 7-3) the question is how to compare them with theoretical COGs in order to obtain all of the parameters listed in the theoretical section. The simplest way to do this is to take a theoretical COG which has a shape similar to that of the experimental COG, and then move the theoretical COG along the x- and y- axis until the two curves coincide, as was suggested by Alkemade [114]. The full coincidence is reached by varying the *a*-parameter. However, this method in generally inaccurate. It provides a satisfactory estimation for $a<1$, where the COGs somewhat differ in shape, but does not work for $a>1$, where the shapes of the COGs do not vary much. For $a<1$ the difference is not pronounced for an uncertainty of $\pm$ 0.1 in the *a*-value. Fig.7-5a shows a set of theoretical COGs which have been calculated using Mathcad software and a polynomial approximation of the integrals in Equation 37 which was proposed by Kuntz [126]. One can see that as *a* becomes greater than 1 (plots 1 through 4 in Figure 7-5a), all plots have the same shape but the intersection point shifts to higher values of n_0fl for higher *a*'s.

The other method to obtain an accurate fit of theoretical COGs to experimental ones is to use duplication curves which relate the duplication factor D to the atomic density [115,125]. D is defined as the relative increase in line intensity I, or integral absorption A_t,

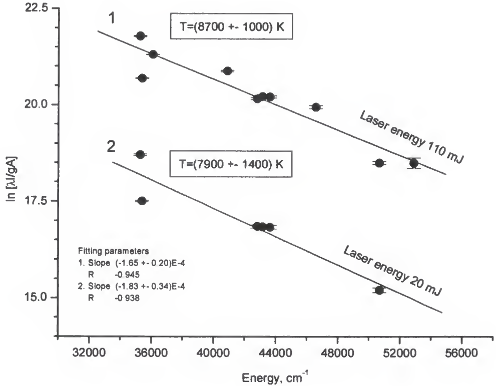

Figure 7-4: Boltzman plots for a laser plasma induced on the steel sample. Iron lines between 423 nm and 431 nm were used. The delay time was 5 μs and the detector gate was 1 μs.

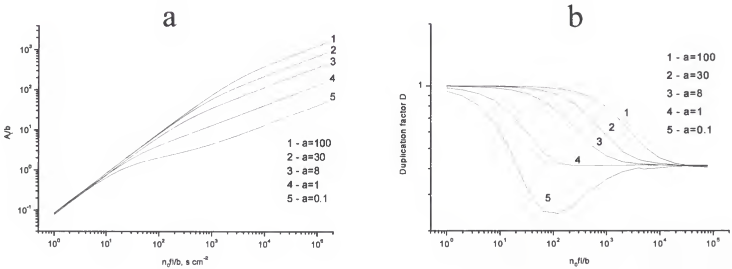

Figure 7-5: a) Theoretical COG calculated by using the Mathcad software and the algorithm proposed in [125]. b) Calculated duplication curves.

caused by a doubling of the product n_0fl:

$$D \equiv \frac{I(2n_0fl) - I(n_0fl)}{I(n_0fl)} \qquad (40).$$

A series of calculated duplication curves is shown in Figure 7-5b. The experimental duplication curve can be obtained either by doubling the concentration (n_0) or the absorption length (l). Once the experimental COG and the duplication curves are available, they can be used together to obtain the exact value of the parameter a [125]. In our experiment, however, we were limited by NIST samples with certain concentrations of Cr, which could not be varied. The approach with doubling the absorption length could not be used in our experimental design due to the top collection scheme of the emission light. We generated semiempirical duplication curves using certified concentration values and experimentally determined linear fit coefficients for the two portions of the calibration plot (with slopes 1 and ½). The result of this simulation is presented in Figure 7-6, where three duplication curves correspond to three values of ablation laser energy. However, this approach was unsatisfactory because the most critical intermediate region of the COG (between the two asymptotes with slopes 1 and ½) could not be modeled due to insufficient data points and thus the generated duplication curves were inaccurate.

We therefore came to the conclusion that some *a priori* knowledge about a likely value of the a-parameter is necessary. In this respect, the measurement of the plasma temperature provides an estimate for a Doppler and a Lorentzian line half-widths via Equations 35 and 36. The Doppler and Lorentzian line half-widths within a broad

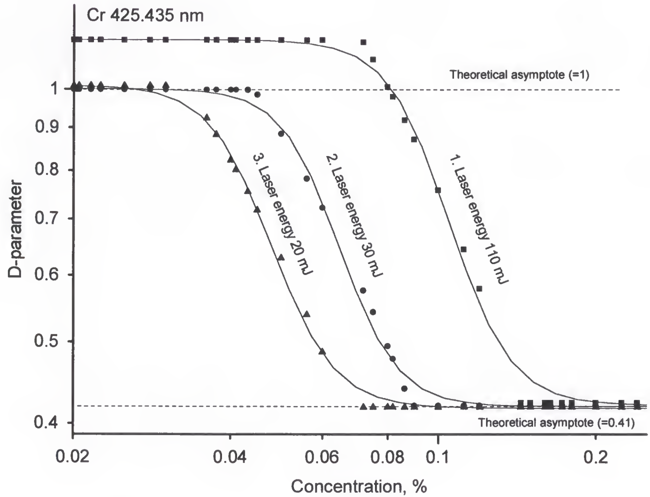

Figure 7-6: Experimental duplication curves for Cr in NIST steel samples.

temperature range are presented in Figure 7-7. In the case of collisional broadening, we assumed that the main collision partner for the Cr atoms was nitrogen (N_2), and the collisional crosssection was taken within a reasonable interval of 50 -100 $Å^2$ as a rough estimate, as recommended in [127]. If we now predict the value for the a-parameter on the basis of the data in Figure 7-4 and the plasma temperature is approximately 8000 K (Fig. 7-7), we obtain $a \approx 0.12$ for a collisional crossection of 50 $Å^2$ and $a \approx 0.24$ for the collisional crossection of 100 $Å^2$. To make this prediction more accurate and to determine how the line width changes with concentration, we measured Cr 425.4 nm line shapes directly by using the frequency doubled narrow band (80 MHz) Ti:Sapphire laser which was scanned across the Cr transition. The resulting line shapes are given in Figure 7-8. The top spectrum represents a purely Doppler-broadened line profile from a low temperature line source (Cr hollow cathode lamp). This profile was measured by using the opto-galvanic technique. The other spectra are line profiles in the laser plasma obtained from samples with different concentrations of Cr. Only one spectrum in this series (0.025 % Cr in steel, second row) was obtained under optically thin plasma conditions when the signal is directly proportional to the concentration (see Figure 7-3). Other spectra were broadened by self-absorption as easily seen in Fig 7-8. If we now compare the line width of the 0.025 % Cr spectrum (4.4 pm) with the Doppler line width (3.8 pm, Figure 7-7) at the estimated plasma temperature of ~8000 K, we find that Doppler broadening is dominant and Lorentzian broadening has only a small contribution to the line shape. The relative contribution of the Doppler and Lorentz profiles to the total line shape may be estimated from the well known values for the Voigt function [128]. In our case, this contribution is equal to 0.86 and 0.26 for Doppler and Lorentz fractions,

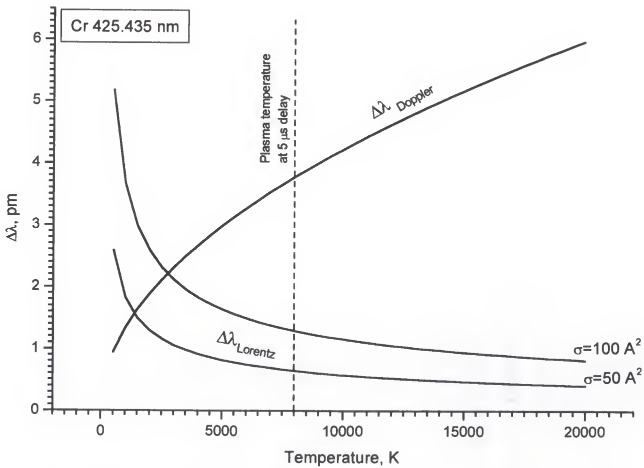

Figure 7-7: Doppler vs Lorentzian broadening in a laser plasma induced in the open air.

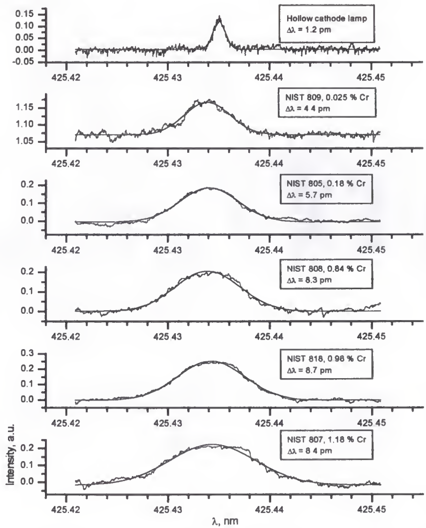

Figure 7-8: Cr 425.435 nm line width in the 800 series NIST standards. Ablation energy is 20 mJ, delay time is 5 μs.

respectively. This provides the value of a-parameter of 0.2, in close agreement with our previous estimates.

Now the theoretical COGs can be compared to the experimental points. The fit of the theoretical COG with a=0.2 to the experimental points, obtained at 5 μs delay time and 20 mJ laser energy (plot 3 in Fig. 7-3), is shown in Figure 7-9. The accuracy of the fit was estimated to be within the values for the a-parameter of 0.20 ± 0.05. It was shown elsewhere [124,128] that the ordinate of the intercept of the two asymptotes is equal to $2a$. In our case, this corresponds to the $n_0 fl/b$ value equal to 5. Now the absolute number density of neutral Cr atoms n_0 can be determined provided that the absorption length l is known. The absorption length was measured by projecting a 1:1 plasma image onto the ICCD camera and calculating the image geometrical size from the number of pixels illuminated. It was found that the plasma size changed with the delay time as shown in Figure 7-10. As seen from Figure 7-10, at a 5 μs delay time, the plasma absorption length is about 2 mm. The oscillator strength f for the Cr 425.4 nm transition is equal to 0.11 [130]. Combining the numerical data, we find that the number density of neutral Cr atoms corresponding to the transition from low to high optical density is equal to 6.5×10^{12} cm^{-3}. This corresponds to the concentration of Cr in the stainless steel matrix to a value between 0.05 and 0.1 Wt %, very close to the results obtained by Leis et al. for Cr in the same samples but under reduced pressure argon atmosphere [131]. Hence, the COG method provides important practical information concerning the linear dynamic range of the calibration and also assists in the choice of lines which should be used in order not to exceed this range.

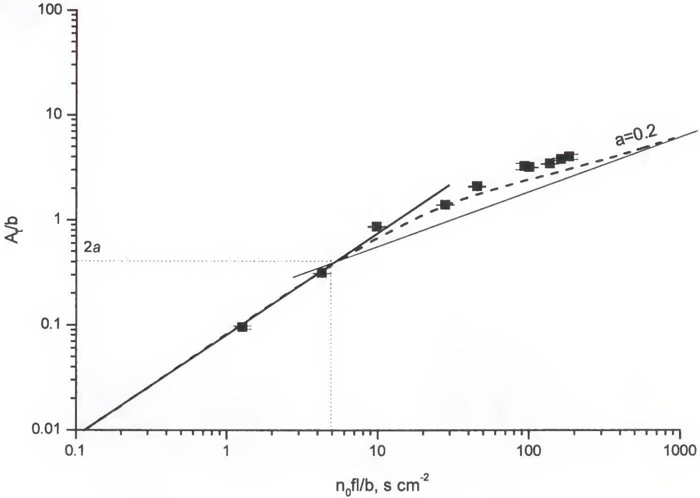

Figure 7-9: Theoretical COG matched to the experimental data points.

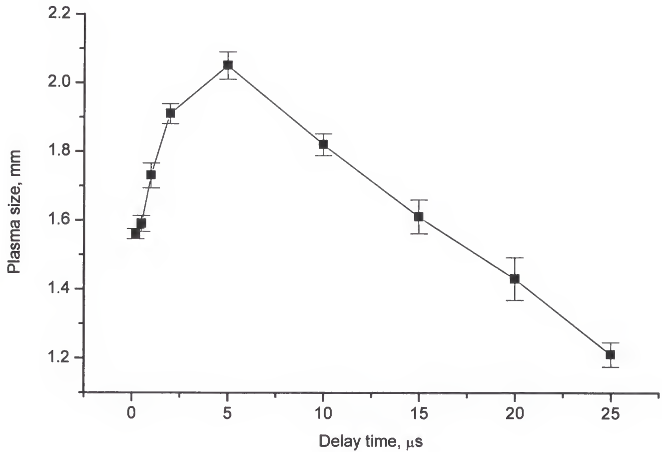

Figure 7-10: Size of the wavelength-integrated plasma image at different delay times.

With the known a-value, we can estimate more precisely the value for the collisional crossection σ using Equation 35. As before, we assume that the laser plasma mainly consists of N_2 molecules. The calculation yields $\sigma = (66 \pm 16)$ Å^2, a quite reasonable value according to the literature data on flame spectroscopy [125,127,129].

Conclusions

Finally, we have to answer the question of how reliable are the results presented in this paper. This question arises because despite the avalanche of publications on LIPS, especially in last few years, the laser plasma is still not very well understood and even the presence of LTE is disputable [132]. Answering this question, we have to note that our value for the a-parameter seems to follow the general trend: the value of a decreases with increasing temperature [113]. Alkemade with co-workers [115,125] have proposed the rate of this change expressed as $a \propto T^{-1.2}$. If we apply this law in order to extrapolate our a-value to the region of well-studied flame temperatures (2500 - 3000 K), we will find typical a-values of 0.6 - 1 for elements like Cr or Mn [115,129]. Furthermore, we note that the collisional broadening crossection obtained in our experiment falls within the same range as in flames [115,125,129] showing the usual weak dependence on temperature. The value of 44 Å^2 reported in [129] for the same Cr line in air-acetylene flame is in reasonable agreement with our value of 66 Å^2 taking into account the difference in temperatures and collisional environments. Overall, we can therefore conclude that the COG method applied to the laser plasma (delayed a few μs after its ignition) is a valuable tool for obtaining both fundamental and analytical spectroscopic information.

CHAPTER 8
CONCLUSIONS AND FUTURE WORK

Laser excited atomic fluorescence spectroscopy and laser source atomic absorption spectroscopy have successfully been used for probing a laser induced plasma. The applicability of these techniques for analyzing solid samples with little or no sample preparation has been demonstrated. The analytical figures of merit for these techniques were evaluated using prepared solid samples as well as NIST certified reference materials.

A procedure for the direct analysis of solid samples for their isotope constituents and concentrations has been developed. A solid lithium oxalate sample was probed with laser ablation and laser excited atomic fluorescence in order to determine the isotope abundance ratio of lithium in the sample. The isotopes of rubidium were resolved and measured using laser source atomic absorption to probe the laser induced plasmas formed on solid samples containing rubidium. The analysis of real geological samples was performed with excellent results. Generally, this technique provides many advantages over the routinely used mass spectrometric techniques for isotope analysis. The LA-LEAFS and LA-LAAS procedures require very little or no sample preparation as compared to the elaborate dissolution techniques which are required by mass spectroscopy. However, the measurement precisions obtained, 4-5%, are slightly worse than the precisions typically obtained by mass spectroscopy of 0.1-2%.

The reason for the comparatively poorer precision was the method of data acquisition used. The isotope ratio of the elements was determined by ratioing the peak heights or peak areas obtained in the spectra; however, each point on the spectrum was measured in successive, different laser plasmas. Therefore, the precision of the isotope ratio measurements reflects the differences in the plasmas because of nonhomogeneity in the sample matrix and the shot-to-shot fluctuations in the ablation laser intensity. Better precision would be expected if each isotope could be probed simultaneously in the same plasma. This would be achieved by replacing the scannable laser system used in this work with two diode lasers, each of which is permanently tuned to one or another isotope transition such that both isotopes are probed simultaneously.

Many other elements could be evaluated with this system in terms of their isotope composition. It would especially be interesting to probe those elements in the middle of the periodic chart which have small isotope shifts. These elements are typically thought unapproachable by spectroscopic techniques because of their small shifts. We have shown, however, that the rubidium line shape is narrower than the Doppler linewidth due to the direction in which the atoms are ejected from the sample surface. Because the atoms are ejected perpendicular to the probe beam, total Doppler broadening is not observed; therefore, it is imaginable that elements with smaller isotope shifts could also be resolved and measured with this technique.

APPENDIX
LIST OF PUBLICATIONS AND PRESENTATIONS

Publications

"A Laser Ablation-Atomic Fluorescence Technique for Isotopically Selective Determination of Lithium in Solids," I. B. Gornushkin, L. A. King, B. W. Smith, and J. D. Winefordner, *Spectrochimica Acta,* **53B**, 1131 (1998).

"Atomic Absorption and Fluorescence Measurements of Rubidium and Potassium in a Laser Induced Breakdown Plasma on a Solid Sample," L. A. King, I. B. Gornushkin, D. Pappas, B. W. Smith, and J. D. Winefordner, in preparation.

"Isotope Analysis of Rubidium in a Laser Induced Plasma," L. A. King, I. B. Gornushkin, D. Pappas, B. W. Smith, and J. D. Winefordner, *Spectrochimica Acta B,* submitted.

"Line Broadening Mechanisms in a Laser Induced Breakdown Plasma,"L. A. King, I. B. Gornushkin, B. W. Smith, and J. D. Winefordner, *Spectrochimica Acta B,* submitted.

"Application of the Curves-of-Growth method for analysis of Chromium in steel," I.B. Gornushkin, J. Anzano, L. King, B. Smith, J. Winefordner, *Spectrochimica Acta B*, submitted.

Presentations

L. A. King, I. B. Gornushkin, D. Pappas, B. W. Smith, and J. D. Winefordner, "Isotope Selective Measurements in a Laser Induced Breakdown Plasma," The 25th Annual Conference of the Federation of Analytical Chemistry and Spectroscopy Societies, Austin, TX, October, 1998.

L. A. King, I. B. Gornushkin, D. Pappas, B. W. Smith, and J. D. Winefordner, "Isotopic Ratio Analysis of Solid Samples by Laser Ablation with Laser Induced Fluorescence and Atomic Absorption," The 49th Pittsburgh Conference of Analytical Chemistry and Applied Spectroscopy, New Orleans, LA, March 1998.

L. A. King, I. B. Gornushkin, D. Pappas, B. W. Smith, and J. D. Winefordner, "Atomic Absorption and Fluorescence of Rubidium in a Laser Induced Plasma on a Solid Sample," The 24th Annual Conference of the Federation of Analytical Chemistry and Spectroscopy Societies, Providence, RI, October 1997.

REFERENCES

1. E. Damon and R. Thomlinson, *Appl. Opt.* **2**, 546 (1963).

2. L. Radziemski and D. Cremers, ed. Laser Induced Plasmas and Applications, Marcel Dekker, Inc., New York (1989).

3. X. Zhao, L. Shen, T. Lu, K. Niemax, *Appl. Phys. B,* **55**, 327 (1992).

4. L. Balazs, R. Gijbels, A. Vertes, *Anal. Chem.* **63**, 314 (1991).

5. Z. Hwang, Y. Teng, K. Li, J. Sneddon, *Appl. Spec.* **45**, 435 (1991).

6. R. Wisbrun, I. Schechter, R. Niessner, H. Schroder, K. Kompa, *Anal. Chem.* **66**, 2964 (1994).

7. R. Pinnick, P. Chylek, M. Jarzembski, E. Creegan, V. Srivastava, G. Fernandez, J. Pendleton, A. Biswas, *Appl. Opt.* **27**, 987, (1988).

8. M. Kuzuya, H. Matsumoto, H. Takechi, O. Mikami, *Appl. Spec.* **47**, 1659 (1993).

9. L. Jensen, S. Langford, J. Dickinson, R. Addleman, *Spectrochim. Acta*, **50B**, 1501 (1995).

10. A. Quentmeier, W. Sdorra, K. Niemax, *Spectrochim. Acta*, **45B**, 537 (1990).

11. D. Rusak, M. Clara, E. Austin, K. Visser, R. Niessner, B. Smith, J. Winefordner, *Appl. Spec.*, **51** 1628 (1997).

12. Y. Lee, S. Sawan, T. Thiem, Y. Teng, J. Sneddon, *Appl. Spec.,* **46**, 436 (1992).

13. R. Measures and H. Kwong, *Appl. Opt.*, **18**, 281 (1979).

14. H. Kwong and R. Measures, *Anal. Chem.* **51**, 428 (1979).

15. A. Lewis, G. Beenen, J. Hosch, and E. Piepmeier, *Appl. Spec.* **37**, 263 (1983).

16. G. Beenen and E. Piepmeier, *Appl. Opt.* **38**, 851 (1984).

17. V. Bondybey, *Science*, **227**, 125 (1985).

18. H. Arlinghaus, W. Calaway, C. Young, M. Pellin, D. Gruen, L. Chase, *J. Appl. Phys.* **65**, 281 (1988).

19. W. Sdorra, A. Quentmeier, K. Niemax, *Mikrochim. Acta,* **II**, 201 (1989).

20. W. Sdorra, A. Quentmeier, K. Niemax, *Atoms, Molecules, and Clusters*, **13**, 95 (1989).

21. A. Quentmeier, W. Sdorra, K. Niemax, *Spectrochim. Acta,* **45B**, 537 (1990).

22. W. Sdorra and K. Niemax, *Spectrochim. Acta*, **45B**, 917 (1990).

23. K. Niemax and W. Sdorra, *Appl. Opt.* **29**, 5000 (1990).

24. W. Sdorra, J. Brust, K. Niemax, *Mikrochim. Acta*, **108**, 1 (1992).

25. Y. Oki, T. Tani, N. Kidera, M. Maeda, *Optics Comm.* **110**, 298 (1994).

26. Y. Oki, K. Furukawa, M. Maeda, *Optics Comm.* **133**, 123 (1997).

27. W. Pesklak and E. Piepmeier, *Mikrochem. Journ.* **50**, 253 (1994).

28. H. Le, R. Dreyfus, W. Marine, M. Sentis, I. Movtchan, *Appl. Sur. Sci.* **96-98**, 164 (1996).

29. D. Zerkle and A. Sappey, *IEEE Trans. on Plasma Sci.* **24**, (1996).

30. R. Neuhauser, U. Panne, R. Niessner, G. Petrucci, P. Cavalli, N. Omenetto, *Anal. Chim. Acta*, **346**, 37 (1997).

31. Y. Oki, K. Matsunaga, T. Nomura, M. Maeda, *Appl. Phys. Lett.* **71**, 2916 (1997).

32. I. Gornushkin, S. Baker, B. Smith, J. Winefordner, *Spectrochim. Acta*, **52B**, 1653 (1997).

33. S. Darke and J. Tyson, *J. Anal. Atomic Spec.*, **8**, 145 (1993).

34. V. Mossotti, K. Laqua, W. Hagenah, *Spectrochim. Acta,* **23B**, 197 (1967).

35. T. Ishizuka, Y. Uwamino, H. Sunahara, *Anal. Chem.,* **49**, 1339 (1977).

36. A. Quentmeier, K. Laqua, W. Hagenah, *Spectrochim. Acta,* **34B**, 117 (1979).

37. A. Quentmeier, K. Laqua, W. Hagenah, *Spectrochim. Acta,* **35B**, 139 (1980).

38. R. Manabe, E. Piepmeier, *Anal. Chem.,* **51**, 2066 (1979).

39. K. Sumino, R. Yamamoto, F. Hatayama, S. Kitamura, *Anal. Chem.*, **52**, 1064 (1980).

40. R. Wennrich and K. Dittrich, *Spectrochim. Acta,* **37B**, 913 (1982).

41. M. Harnafi and B. Dubreuil, *J. Appl. Phys.*, **69**, 7565 (1991).

42. M. Tanaka, Y. Fujisawa, T. Nakajima, T. tasaka, K. Ota, S. Usami, *J. Appl. Phys.,* **83**, 3379 (1998).

43. J. Goleb, *Anal. Chim. Acta,* **34**, 135 (1966).

44. J. Wheat, *Appl. Spec.,* **25**, 328 (1971).

45. A. Meier, *Anal. Chem.,* **54**, 2158 (1982).

46. H. Gibbs and G. Churchill, *J. Opt. Soc. America,* **62**, 1130 (1972).

47. J. Gustafsson, D. Rojas, O. Axner, *Spectrochim. Acta,* **52B**, 1937 (1997).

48. K. Song, E. Jung, H. Cha, J. Lee, M. Kim, S. Lee, *J. Anal. Atomic Spec.*, **13**, 301 (1998).

49. A. Obrebski, J. Lawrenz, K. Niemax, *Spectrochim. Acta,* **45B**, 15 (1990).

50. K. Niemax, H. Groll, C. Patschan, *Spectrochim. Acta Rev.,* **15**, 349 (1993).

51. H. Wizeman and K. Niemax, *Mikrochim. Acta,* **129**, 209 (1998).

52. H. Wizeman and K. Niemax, *Anal. Chem.*, **69**, 4291 (1997).

53. H. Niki, T. Yasuda, I. Kitazima, *J. Nucl. Sci. Tech.*, **35**, 34 (1998).

54. W. Pietsch, A. Petit, A. Briand, *Spectrochim. Acta,* **53B**, 751 (1998).

55. B. Smith, A. Quentmeier, M. Bolshov, K. Niemax, *Spectrochim. Acta Part B,* in press (1999).

56. R. Frei and T. Pettke, *Geology*, **24**, 823 (1996).

57. H. Schleicher, W. Todt, S. Viladkar, F. Schmidt, *Chem. Geology*, **140**, 261 (1997).

58. J. Woodhead and J. Hergt, *Chem. Geology*, **138**, 311 (1997).

59. E. Barg, D. Lal, M. Pavich, M. Caffee, J. Southon, *Chem. Geology*, **140**, 237 (1997).

60. A. Bechtel, W. Elliott, S. Oszczepalski, *Economic Geology,* **91**, 1310 (1996).

61. D. Brandt, W. Reimold, C. Smith, *S. African J. Geology,* **99**, 293 (1996).

62. K. Krauskopf and D. Bird, Introduction to Geochemistry, McGraw Hill, Inc., New York (1995).

63. W. Kinard, N. Bibler, C. Coleman, S. Wyrick, *Radiochim. Acta,* **66/67**, 259 (1994).

64. A. Espartero, J. Suarez, M. Rodriguez, *Appl. Radiat. Isot.,* **49**, 1277 (1998).

65. G. Russ and J. Bazan, *Spectrochim. Acta*, **42B**, 49 (1987).

66. G. Choppin, J. Rydberg, J. Liljenzin, ed., Radiochemistry and Nuclear Chemistry, Butterworth-Heinemann Ltd., Boston (1995).

67. K. Lieser, Nuclear and Radiochemistry: Fundamentals and Applications, VCH, New York (1997).

68. P Atkins, Physical Chemistry, 4th ed., W. H. Freeman and Company, New York (1990).

69. A. Thorne, Spectrophysics, Chapman and Hall, New York (1988).

70. W. Pauli and R. Peierls, *Phys. Z*, **32**, 670 (1931).

71. H. Kuhn, Atomic Spectra, Academic Press, New York (1963).

72. C. Alkemade, T. Hollander, W. Snelleman, P. Zeegers, Metal Vapours in Flames, Pergamon Press, New York (1982).

73. J. Ingle and S. Crouch, Spectrochemical Analysis, Prentice Hall Inc., Englewood Cliffs (1988).

74. A. Radzig and B. Smirnov, Reference Data on Atoms, Molecules, and Ions, Springer-Verlag, New York (1985).

75. K. Wedepohl, ed. Handbook of Geochemistry, Springer-Verlag, New York (1970).

76. A. Levenson, Introduction to Exploration Geochemistry, Applied Publishing Ltd., Maywood (1974).

77. K. Olive and D. Schramm, *Nature*, **360**, 439 (1992).

78. W. Seyfried, D. Janecky, M. Mattl, *Geochim. Cosmochim. Acta*, **48**, 557 (1984).

79. L. Chan, J. Gieskes, C. You, J. Edmond, *Geochim. Cosmochim. Acta,* **58**, 4443 (1994).

80. T. Xiao, H. Qi, Y. Wang, L. Jin, *Chinese Sci. Bull.,* **37**, 469 (1992).

81. D. Gregoire, B. Acheson, R. Taylor, *J. Anal. Atom. Spectrosc.,* **11**, 765 (1996).

82. A. Meier, *Anal. Chem.,* **54**, 2158 (1982).

83. J. Wheat, *Appl. Spec.,* **25**, 328 (1971).

84. H. Rade, *Atomic Abs. Newslett.,* **13**, 81 (1974).

85. A. Walsh, *Spectrochim. Acta,* **7B**, 108 (1955).

86. A. Zaidel and E. Korennoi, *Optics and Spectroscopy,* **10**, 299 (1961).

87. I. Gornushkin, S. Baker, B. Smith, J. Winefordner, *Spectrochim. Acta,* **52B**, 1653 (1997).

88. I. Gornushkin, J. Kim, B. Smith, S. Baker, J. Winefordner, *Appl. Spec.,* **51**, 1055 (1997).

89. D. Lide, ed., Handbook of Chemistry and Physics, CRC Press, Inc., Boston (1990).

90. M. Whitehouse and J. Russell, *Chemical Geology,* **136**, 295 (1997).

91. E. Barg, D. Lal, M. Pavich, M. Caffee, J. Southon, *Chemical Geology,* **140**, 237 (1997).

92. R. Frei and T. Pettke, *Geology*, **24**, 823 (1996).

93. A. Espartero, J. Suarez, M. Rodriguez, *Appl. Rad. and Isotopes,* **49**, 1277 (1998).

94. R. Breckenridge and A. Crockett, *Environmental Monitoring and Assessment,* **51**, 621 (1998).

95. C. Zeissler, S. Wright, R. Lindstrom, *Appl. Rad. and Isotopes,* **49**, 1091 (1998).

96. E. B. Salomen, *Spectrochim. Acta,* **49B**, 1139 (1993).

97. W. Kinard, N. Bibler, C. Coleman, S. Wyrick, *Radiochim. Acta,* **66/67**, 259 (1994).

98. I. Gornushkin, S. Baker, B. Smith, J. Winefordner, *Spectrochim. Acta,* **52B**, 1653 (1997).

99. J. Aguilera, C. Aragon, J. Campus, *Appl. Spec.,* **46**, 1382 (1992).

100. M. Sabsabi, P. Crelo, S. Boily, M. Chaker, *SPIE*, **2069**, 191 (1993).

101. H. Niki, T. Yasuda, I. Kitazima, *J. of Nuclear Science and Technology,* **35**, 34 (1998).

102. W. Pietsch, A. Petit, A. Briand, *Spectrochim. Acta,* **53B**, 751 (1998).

103. K. Niemax, H. Groll, C. Schnurer-Patschan, *Spectrochim. Acta Rev.,* **15**, 349 (1993).

104. M. Harnafi, B. Dubreuil, *J. Appl. Phys.,* **69**, 7565 (1991).

105. H. Wizeman and K. Niemax, *Mikrochim. Acta,* **129**, 209 (1998).

106. H. Wizeman and K. Niemaz, *Anal. Chem.,* **69**, 4291 (1997).

107. W. Lochte-Holtgreven, ed., Plasma Diagnostics, John Wiley and Sons, Inc., New York (1968).

108. Parsons, Smith, Bentley, Handbook for Flame Spectroscopy, Plenum Press, New York (1975).

109. X. Zhao, L. Shen, T. Lu, K. Niemax, *Appl. Phys. B,* **55**, 327 (1992).

110. N. Omenetto, J. Bower, J. Bradshaw, C. Dijik, *J. Quant. Spectrosc. Radiat. Transfer,* **24**, 147 (1980).

111. R. Von Ladenburg and F. Reiche, *Ann. D. Phys.* **42**, 181 (1913).

112. A.C.G. Mitchell and M.W. Zemansky, Resonance Radiation and Excited Atoms, Cambridge University Press, London (1934).

113. Von E.F.M. van der Held, *Zeitschrift fur Physic,* **70**, 508 (1931).

114. E. Hinnov, *J. Opt. Soc. Am.* **47**, 151 (1957).

115. C.Th.J. Alkemade, Tj. Hollander, W. Snelleman, P.J.T. Zeegers, Metal Vapours in Flames, Pergamon Press, New York (1982).

116. Tj. Hollander, "Self-Absorption, Ionization and Dissociation of Metal Vapours in Flames", Ph.D. Thesis, Utrecht, Netherlands.

117. P.J.T. Zeegers, R. Smith, and J.D. Winefordner, *Anal. Chem.* **40**, 26A (1968).

118. T.J. Vickers, L.D. Remington, and J.D. Winefordner, *Anal. Chim. Acta* **36**, 42 (1966).

119. B.W. Smith, M.J. Rutledge, and J.D. Winefordner, *Appl. Spec.* **41**, 613 (1987).

120. B.J. Jansen and Tj. Hollander, *Spectrochim. Acta* **32B**, 165 (1977).

121. C.F. Hansen and R.L. McKenzie, *J. Quant. Spectrosc. Radiat. Transfer* **11**, 349 (1971).

122. F. Schreier, *J. Quant. Spectrosc. Radiat. Transfer* **48**, 743 (1992).

123. G. Canalizo, G. Koenigsberger, D. Peña, and E. Ruiz, *Revista Mexicana de Astronomía y Astrofisíca* **31**, 63 (1995).

124. R. Mavrodineanu and H. Boiteax, Flame Spectroscopy, John Wiley, New York (1965).

125. C. van Trigt, Tj. Hollander, and C.T.J. Alkemade, *J. Quant. Spectrosc. Radiat. Transfer,* **5**, 813 (1965).

126. M. Kuntz, *J. Quant. Spectrosc. Radiat. Transfer* **57**, 819 (1997).

127. M.L. Parsons, B.W. Smith, and G.E. Bentley, Handbook of Flame Spectroscopy, Plenum Press, New York (1975).

128. W. Lochte-Holtgreven, Plasma Diagnostics, North-Holland Publishing Company - Amsterdam (1968).

129. E. Hinnov and H. Kohn, *J. Opt. Soc. Am.* **47**, 156 (1957).

130. Astrophysics Data System, NIST Atomic Spectroscopic Database, http://aeldata.nist.gov.

131. F. Leis, W. Sdorra, J.B. Ko, and K. Niemax, *Mikrochim. Acta* [Wien] **II**, 185 (1989).

132. B.C. Castle, K. Visser, B.W. Smith, and J.D. Winefordner, *Spectrochim. Acta* **52B**, 1995 (1997).

BIOGRAPHICAL SKETCH

Leslie Anthony King was born in Columbus, Georgia, on August 17, 1972. She is the oldest of two sisters. She was raised in Reynolds, Georgia, and attended Taylor County High School. Leslie received her Bachelor of Science degree with a major in chemistry and a minor in mathematics from Georgia College in Milledgeville, Georgia on June 11, 1994. She entered graduate school at the University of Florida in August, 1994, and joined Graduate Research Professor Jim Winefordner's research group to work on her doctoral degree in analytical chemistry.

I certify that I have read this study and that in my opinion it conforms to acceptable standards of scholarly presentation and is full adequate, in scope and quality, as a dissertation for the degree of Doctor of Philosophy.

James D. Winefordner

James D. Winefordner, Chairman
Graduate Research Professor of Chemistry

I certify that I have read this study and that in my opinion it conforms to acceptable standards of scholarly presentation and is full adequate, in scope and quality, as a dissertation for the degree of Doctor of Philosophy.

W. W. Harrison

Willard W. Harrison
Professor of Chemistry

I certify that I have read this study and that in my opinion it conforms to acceptable standards of scholarly presentation and is full adequate, in scope and quality, as a dissertation for the degree of Doctor of Philosophy.

Samuel O. Colgate

Samuel O. Colgate
Professor of Chemistry

I certify that I have read this study and that in my opinion it conforms to acceptable standards of scholarly presentation and is full adequate, in scope and quality, as a dissertation for the degree of Doctor of Philosophy.

David E. Richardson

David Richardson
Professor of Chemistry

I certify that I have read this study and that in my opinion it conforms to acceptable standards of scholarly presentation and is full adequate, in scope and quality, as a dissertation for the degree of Doctor of Philosophy.

Joseph J. Delfino
Professor of Environmental Engineering Sciences

This dissertation was submitted to the Graduate Faculty of the Department of chemistry in the College of Liberal Arts and Sciences and to the Graduate School and was accepted as partial fulfillment of the requirements for the degree of Doctor of Philosophy.

December 1998

Dean, Graduate School